Icarus 369 (2021) 114594

Contents lists available at ScienceDirect

Icarus

journal homepage: www.elsevier.com/locate/icarus

Research Paper

Ephemeris and hazard assessment for near-Earth asteroid (101955) Bennu based on OSIRIS-REx data

Davide Farnocchia [a,*], Steven R. Chesley [a], Yu Takahashi [a], Benjamin Rozitis [b], David Vokrouhlický [c], Brian P. Rush [a], Nickolaos Mastrodemos [a], Brian M. Kennedy [a], Ryan S. Park [a], Julie Bellerose [a], Daniel P. Lubey [a], Dianna Velez [a], Alex B. Davis [a], Joshua P. Emery [d], Jason M. Leonard [e], Jeroen Geeraert [e], Peter G. Antreasian [e], Dante S. Lauretta [f]

[a] Jet Propulsion Laboratory, California Institute of Technology, Pasadena, CA 91109, USA
[b] The Open Universit, Milton Keynes MK7 6AA, UK
[c] Institute of Astronomy, Charles University, CZ-18000 Prague 8, Czech Republic
[d] Department of Astronomy and Planetary Science, Northern Arizona University, Flagstaff, AZ 86011, USA
[e] KinetX Aerospace, Simi Valley, CA 93065, USA
[f] Lunar and Planetary Laboratory, University of Arizona, Tucson, AZ 85721, USA

ARTICLE INFO

Dataset link: https://sbn.psi.edu/pds/resource/orex/, http://sbmt.jhuapl.edu/, https://naif.jpl.nasa.gov/pub/naif/ORX/

Keywords:
Asteroids
Dynamics
Celestial mechanics
Near-Earth objects
Orbit determination

ABSTRACT

Small bodies such as the near-Earth asteroid Bennu drift in their orbit due to thermal radiation forces (the Yarkovsky effect). Ground-based observations have indicated a nonzero probability of Bennu impacting Earth, depending on how its orbit evolves. Thus, among the goals of the OSIRIS-REx (Origins, Spectral Interpretation, Resource Identification, and Security-Regolith Explorer) mission to Bennu were to precisely measure the Yarkovsky effect and refine the impact hazard assessment for this body. Here we address these objectives. Using OSIRIS-REx spacecraft tracking data, we derive meter-level constraints on the distance between Earth and Bennu from January 2019 to October 2020. While these data greatly improve the knowledge of the trajectory of Bennu, they also require an unprecedented fidelity for the modeling of an asteroid's trajectory. In particular, special care is needed to take into account the contribution of 343 small-body perturbers and the uncertainty in their masses. Radiation effects such as the Poynting–Robertson drag, so far only considered for interplanetary dust dynamics, now become a consideration for modeling the trajectory of a 500-m asteroid such as Bennu. By employing a thermophysical model based on OSIRIS-REx's characterization of Bennu, we estimate a semimajor axis drift of -284.6 ± 0.2 m/yr (signal-to-noise ratio ~1400) at epoch 2011 January 1 caused by the Yarkovsky effect. The largest source of modeling error is solar wind drag, which may lower the magnitude of the semimajor axis drift from the Yarkovsky effect by up to 0.16 m/yr. The Yarkovsky-related semimajor axis drift varies by roughly ± 1 m/yr as the orbit of Bennu evolves due to planetary perturbations from 1900 to 2135. The Yarkovsky thermophysical model proves to be extremely accurate by predicting a bulk density estimate within 0.1% of that estimated through gravity science analysis. Compared to the information available before the OSIRIS-REx mission, the knowledge of the circumstances of the scattering Earth encounter that will occur in 2135 improves by a factor of 20, thus allowing us to rule out many previously possible impact trajectories. However, there remain some impact trajectories compatible with the data. Prior to the spacecraft encounter, the overall impact probability through 2200 was 3.7×10^{-4} (1 in 2700). As a result of our analysis, the cumulative impact probability through 2300 becomes 5.7×10^{-4} (1 in 1750) and the most significant individual impact solution is for September 2182, with an impact probability of 3.7×10^{-4} (1 in 2700). Both Bennu and (29075) 1950 DA have a Palermo scale value of −1.42 and share the distinction as the currently most hazardous object in the asteroid catalog.

* Corresponding author.
E-mail address: davide.farnocchia@jpl.nasa.gov (D. Farnocchia).

https://doi.org/10.1016/j.icarus.2021.114594
Received 17 March 2021; Received in revised form 14 June 2021; Accepted 20 June 2021
Available online 10 August 2021

1. Introduction

Near-Earth asteroid (101955) Bennu is a potentially hazardous asteroid that was discovered in 1999 by the Lincoln Near-Earth Asteroid Research Team (MPEC 1999-R44).[1] Since its discovery, Bennu has been extensively tracked with 580 ground-based optical astrometric observations[2] through 2018. The orbital period of 1.2 yr puts Bennu close to a 6:5 mean motion resonance with Earth, which has led to three close encounters in 1999, 2005, and 2011. During these encounters the Arecibo and Goldstone radar stations collected seven Doppler and 22 delay measurements of Bennu.[3] For a general description of radar astrometry see Yeomans et al. (1987), Ostro et al. (2002). This wealth of ground-based tracking data allows an extremely accurate description of Bennu's motion (Chesley et al., 2014). The trajectory of Bennu is deterministic until 2135, when a close encounter with Earth leads to strong scattering and makes the knowledge of its future motion statistical. In particular, Chesley et al. (2014) found several possible impacts from 2175 to 2196 for a cumulative impact probability of 3.7×10^{-4}.

As recognized by Milani et al. (2009), a key consideration in modeling the trajectory of Bennu and assessing its impact hazard is the Yarkovsky effect, a subtle recoil acceleration due to anisotropically emitted thermal radiation that causes a drift in semimajor axis (Vokrouhlický et al., 2015). From ground-based optical and radar astrometry, Chesley et al. (2014) found that the Yarkovsky-driven semimajor axis drift for Bennu is $da/dt = -283.8 \pm 1.5$ m/yr, by far the Yarkovsky detection in the asteroid catalog with the highest signal-to-noise ratio (Farnocchia et al., 2013; Chesley et al., 2016; Del Vigna et al., 2018; Greenberg et al., 2020). By comparing the measured Yarkovsky effect and the independent thermophysical model based on the physical properties of Bennu as derived from radar observations (Nolan et al., 2013) and Spitzer thermal data (Emery et al., 2014), Chesley et al. (2014) derived a bulk density of 1260 ± 70 kg/m^3, corresponding to $GM = 5.2 \pm 0.6$ m^3/s^2. Scheeres et al. (2019) refined the GM estimate by adopting a first Yarkovsky model directly based on OSIRIS-REx (Origins, Spectral Interpretation, Resource Identification, and Security-Regolith Explorer) data and obtaining $GM = 4.9 \pm 0.1$ m^3/s^2.

The OSIRIS-REx spacecraft arrived at Bennu in December 2018 (Lauretta et al., 2019a, and references therein) and performed the Touch-and-Go (TAG) sample acquisition maneuver in October 2020, achieving the mission's primary objective of collecting a sample of carbonaceous regolith to return to Earth (Lauretta et al., 2017, 2021; Lauretta and OSIRIS-REx TAG Team, 2021). Among the other goals of the OSIRIS-REx mission are improving the knowledge of the future trajectory of Bennu and reassessing the possibility of an impact on Earth. A related goal is to obtain a full characterization of the Yarkovsky effect, by acquiring all the data needed to develop and validate a high-fidelity thermophysical model of the Yarkovsky perturbation and refine the measurement of the related semimajor axis drift (Lauretta et al., 2017).

An early glimpse of the power of the OSIRIS-REx data for constraining the trajectory of Bennu was given by the optical navigation images collected as the spacecraft approached the asteroid in late 2018, which shrank prediction uncertainties for 2135 by a factor of 3 (Farnocchia et al., 2019). A validation of the Yarkovsky model used by Chesley et al. (2014) comes from the mass of Bennu as measured from longer-term datasets tracking both the OSIRIS-REx spacecraft and particles naturally ejected from the surface of Bennu: $GM = 4.8904 \pm 0.0009$ m^3/s^2 (Scheeres et al., 2020a; Chesley et al., 2020). In this paper, we leverage the full OSIRIS-REx tracking dataset acquired over almost two years of proximity operations at Bennu to refine the estimate of the Yarkovsky effect acting on Bennu and the probability of a future impact with Earth.

[1] https://www.minorplanetcenter.org/mpec/J99/J99R44.html.

[2] https://www.minorplanetcenter.org/db_search/show_object?utf8=?&object_id=Bennu.

[3] https://ssd.jpl.nasa.gov/?grp=num&fmt=html&radar=.

2. OSIRIS-REx tracking and constraints on the orbit of Bennu

OSIRIS-REx X-band radiometric (Thornton and Border, 2003) and optical navigation (Owen, 2011) tracking data acquired during asteroid proximity operations provide invaluable information on the ephemeris of Bennu from arrival in December 2018 to TAG in October 2020. Ranging to orbiting spacecraft has been widely used for planetary ephemeris estimation (e.g., Folkner et al., 2014) because it provides a tight constraint on the distance between Earth and a target body.

We considered the orbital phases of the mission where the OSIRIS-REx spacecraft was in a closed orbit about Bennu. These phases include Orbital A, B, C, and R, as well as orbital episodes during the Reconnaissance B and C, Rehearsal, and pre-TAG phases (Lauretta et al., 2017).[4] Within each phase, we selected independent, maneuver-free arcs of about 10 days and estimated the trajectory of the OSIRIS-REx spacecraft by fitting Doppler and optical navigation data, and excluding range data. The configuration of the spacecraft orbit determination filter is analogous to the one used for deriving the spacecraft gravity field solution in Scheeres et al. (2020a). We inflated the a priori uncertainty of the Bennu ephemeris by orders of magnitude relative to current knowledge (solution 103, Farnocchia et al., 2018, 2019). This inflation was meant to reduce possible correlations between the different arcs.

For each arc, we selected a high-gain antenna range pass corresponding to a time when the OSIRIS-REx spacecraft position relative to Bennu was known at the ∼1 m level, based on the formal 1-σ uncertainty and the comparison to the navigation team trajectory estimates.[5] Then, we computed the roundtrip light time from the geocenter to the Bennu barycenter, corrected by the relativistic effect of the Sun (Moyer, 2003, Sec. 8). Finally, we constructed a geocentric pseudo-range point by adding the median residuals of the selected range pass, which we corrected for elevation-specific effects due to the troposphere of Earth (Standish, 1990) that do not apply for a geocentric reduction. On the other hand, the pseudo-range points are not corrected for solar plasma effects (Standish, 1990; Folkner and Kahn, 1992; Moyer, 2003), which are especially significant at small solar elongations and which we model as part of the Bennu orbit fitting process. The added residual corresponds to the range between the Deep Space Network (DSN) tracking station and the OSIRIS-REx spacecraft, not the range between geocenter and Bennu barycenter. However, the change in geometry between the two configurations has a negligible effect in the residual (e.g., see Farnocchia et al., 2021). Table 1 lists the pseudo-range points generated, for which we assume an uncertainty of 15 ns. This uncertainty corresponds to about 2 m and accounts for both spacecraft position error (<1 m) and the typical 1–2 m per-pass range bias (Thornton and Border, 2003; Konopliv et al., 2014, also consistent with the observed scatter of OSIRIS-REx per-pass range residuals in our fits).

3. Modeling the trajectory of Bennu

The pseudo-range points of Table 1 greatly improve the knowledge of the trajectory of Bennu. At the same time, they require an unprecedented fidelity for the modeling of an asteroid's trajectory to be accurate enough to fit them.

3.1. Gravitational forces

We integrated the trajectory of Bennu relative the Solar System barycenter based on JPL planetary ephemeris DE424 (Folkner, 2011), which is the one adopted by the OSIRIS-REx mission.[6] The force model is based on a first-order parametrized post-Newtonian N-body

[4] https://www.asteroidmission.org/asteroid-operations/.

[5] https://naif.jpl.nasa.gov/pub/naif/ORX/kernels/spk/.

[6] https://naif.jpl.nasa.gov/pub/naif/ORX/kernels/spk/de424.bsp.

Table 1
Geocentric pseudo-range points for the Bennu barycenter as derived from OSIRIS-REx high-gain antenna tracking data. Each pseudo-range point represents the roundtrip light time from the geocenter to the Bennu barycenter corrected by solar relativistic effects. The uncertainty is 15 ns, corresponding to about 2 m. The pseudo-range points are affected by solar plasma effects, which need to be modeled as part of the Bennu orbit fitting process.

Time UTC	Round-trip delay s	Frequency MHz	DSN station	Arc	Mission phase
2019-01-03 16:56:56	704.936460063	7188.3	DSS 65	2019-01-01 to 2019-01-10	Orbital A
2019-01-16 16:18:02	655.959459878	7188.3	DSS 55	2019-01-10 to 2019-01-20	Orbital A
2019-01-27 16:17:43	617.519120092	7188.3	DSS 65	2019-01-20 to 2019-01-30	Orbital A
2019-02-03 16:17:32	596.159350117	7188.4	DSS 54	2019-01-30 to 2019-02-09	Orbital A
2019-02-11 16:17:22	575.846395776	7188.4	DSS 65	2019-02-09 to 2019-02-19	Orbital A
2019-02-24 16:27:11	554.804827167	7188.4	DSS 63	2019-02-19 to 2019-02-28	Orbital A
2019-06-19 15:54:34	1064.545480294	7188.8	DSS 55	2019-06-12 to 2019-06-25	Orbital B
2019-07-04 17:21:14	1174.343703031	7188.8	DSS 54	2019-06-28 to 2019-07-08	Orbital B
2019-07-14 17:34:29	1246.401122971	7188.8	DSS 65	2019-07-08 to 2019-07-17	Orbital B
2019-07-24 16:18:22	1316.376058566	7188.8	DSS 55	2019-07-17 to 2019-07-27	Orbital B
2019-08-03 16:31:05	1384.511410774	7188.8	DSS 65	2019-07-27 to 2019-08-06	Orbital B
2019-08-14 17:27:43	1455.997142713	7188.7	DSS 55	2019-08-09 to 2019-08-18	Orbital C
2019-08-23 17:07:16	1510.862317945	7188.7	DSS 54	2019-08-18 to 2019-08-29	Orbital C
2019-09-02 16:14:15	1567.722979226	7188.7	DSS 63	2019-08-29 to 2019-09-06	Orbital C
2019-09-13 16:09:34	1624.831333335	7188.7	DSS 65	2019-09-06 to 2019-09-17	Orbital C
2019-11-05 15:56:18	1802.127387697	7188.5	DSS 65	2019-11-01 to 2019-11-12	Orbital R
2019-11-18 16:03:36	1818.192590338	7188.5	DSS 54	2019-11-12 to 2019-11-23	Orbital R
2019-11-27 16:11:37	1822.972436595	7188.5	DSS 55	2019-11-23 to 2019-12-04	Orbital R
2019-12-08 15:00:57	1821.821951830	7188.5	DSS 55	2019-12-04 to 2019-12-15	Orbital R
2019-12-19 16:08:42	1813.446892154	7188.4	DSS 54	2019-12-15 to 2019-12-26	Orbital R
2019-12-30 16:18:47	1798.494791819	7188.4	DSS 63	2019-12-26 to 2020-01-05	Orbital R
2020-01-08 16:36:16	1781.742550207	7188.4	DSS 54	2020-01-05 to 2020-01-14	Orbital R
2020-01-28 16:38:43	1733.227222480	7188.4	DSS 55	2020-01-22 to 2020-02-04	Recon/Rehearsal
2020-02-17 17:01:03	1674.602445261	7188.4	DSS 65	2020-02-12 to 2020-02-25	Recon/Rehearsal
2020-03-17 16:25:49	1590.941158422	7188.4	DSS 55	2020-03-12 to 2020-03-25	Recon/Rehearsal
2020-03-30 16:25:35	1561.831353581	7188.4	DSS 55	2020-03-25 to 2020-04-07	Recon/Rehearsal
2020-05-04 15:25:28	1538.690576243	7188.5	DSS 63	2020-04-30 to 2020-05-09	Recon/Rehearsal
2020-05-15 16:25:30	1552.190152759	7188.6	DSS 63	2020-05-09 to 2020-05-19	Recon/Rehearsal
2020-05-30 16:25:47	1586.764099189	7188.6	DSS 63	2020-05-27 to 2020-06-06	Recon/Rehearsal
2020-06-14 17:15:48	1637.974503047	7188.6	DSS 55	2020-06-06 to 2020-06-16	Recon/Rehearsal
2020-07-15 18:49:33	1781.082318563	7188.7	DSS 55	2020-07-09 to 2020-07-22	Recon/Rehearsal
2020-07-27 15:12:01	1842.992175656	7188.7	DSS 65	2020-07-22 to 2020-08-04	Recon/Rehearsal
2020-09-04 19:48:09	2045.282059309	7188.7	DSS 26	2020-08-27 to 2020-09-07	TAG
2020-09-13 15:43:38	2086.292417952	7188.7	DSS 65	2020-09-07 to 2020-09-17	TAG
2020-09-25 19:04:08	2137.763679992	7188.6	DSS 25	2020-09-17 to 2020-09-27	TAG
2020-10-03 19:14:18	2168.084119620	7188.6	DSS 26	2020-09-27 to 2020-10-06	TAG

formulation (also referred to as Einstein–Infeld–Hoffman formulation, Moyer, 2003; Will, 1993) for the Sun, the eight planets, Pluto, and the Moon. As already shown by Chesley et al. (2014), a simpler relativistic formulation that only accounted for the term of the Sun would lead to an inaccurate estimate of the Yarkovsky effect. Moreover, we added the point-mass Newtonian gravitational acceleration from the 343 perturbers used for JPL planetary ephemerides DE430 and DE431 (Folkner et al., 2014).

When Bennu is within 1 au of Earth, we included the oblateness term (J_2) in the geopotential of Earth (Kaula, 1966). Higher order terms have a negligible effect (Farnocchia et al., 2017a) at the distances at which Bennu has approached Earth since its discovery.

3.2. Yarkovsky effect

The Yarkovsky effect is a crucial component of the force model for Bennu. The simplest approach to model the Yarkovsky perturbation is a pure transverse acceleration that fully captures the semimajor axis drift (Farnocchia et al., 2013). While this simple formulation can work to fit the ground-based optical and radar astrometry of Bennu (Chesley et al., 2014) it proves inadequate with the constraints coming from OSIRIS-REx tracking and cannot match the meter-level pseudo-range points of Table 1.

Chesley et al. (2014) employed two thermophysical models for the Yarkovsky effect. The first model is referred to as *linear model*, approximates the asteroid as a sphere, and is based on a linearized solution of the heat-transfer equation (Vokrouhlický et al., 2000). We updated this model to use the equivalent radius (246 m, Scheeres et al., 2019) and spin pole (R.A. = 85.46°, Dec. = −60.36°)[7] of Bennu as measured by OSIRIS-REx. The second, higher-fidelity model employed by Chesley et al. (2014) is referred to as the *nonlinear model* and is based on a nonlinear, iterative solution of the heat-transfer problem for a finite-element mesh of facets for the asteroid's shape for a frozen orbit (Čapek and Vokrouhlický, 2005). We used the 12,000-facet version of the v34 shape model[8] derived from a combination of stereophotoclinometry and laser ranging (Barnouin et al., 2020) and computed the Yarkovsky acceleration as a lookup table in true anomaly and the other orbital parameters. The grid encompasses the orbital element variations through the year 2135 and is interpolated to compute the acceleration as a function of the instantaneous orbit. In our setup, both models depend on two parameters: bulk density and thermal inertia of Bennu.

The third Yarkovsky model we used in this work is the detailed thermophysical model of Bennu derived from the characterization performed by OSIRIS-REx (Rozitis et al., 2020). This model is based on the Advanced Thermophysical Model developed by Rozitis and Green (2011, 2012, 2013) and is similar to the non-linear model of Čapek and Vokrouhlický (2005) but includes the additional effects of rough surface thermal-infrared beaming. These beaming effects cause absorbed solar radiation to be re-emitted back towards Sun and result in a general enhancement of the induced Yarkovsky orbital drift by directing more thermally emitted photons into Bennu's orbital plane, particularly in the radial direction (see Fig. 1). Rozitis et al. (2020)

[7] https://naif.jpl.nasa.gov/pub/naif/ORX/kernels/pck/bennu_v16.tpc.

[8] The v34 shape model is available at http://sbmt.jhuapl.edu/Object-Template.php?obj=77.

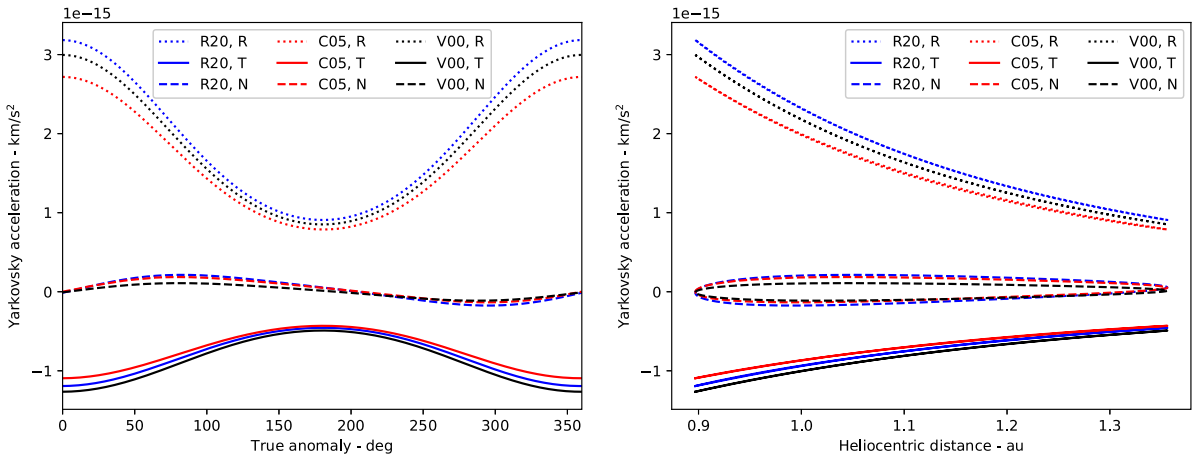

Fig. 1. Yarkovsky acceleration in the radial (R), transverse (T), and out-of-plane (N) component as a function of true anomaly (left panel) and heliocentric distance (right panel). The three Yarkovsky models used are from Vokrouhlický et al. (2000, V00), Čapek and Vokrouhlický (2005, C05), and Rozitis et al. (2020, R20). The bulk density of Bennu is set to 1190 kg/m^3 (Scheeres et al., 2019). In the C05 and V00 models, the thermal inertia is set to 300 J m^{-2} s$^{-0.5}$ K^{-1} (Rozitis et al., 2020).

constrained both thermal inertia and surface roughness in the model by fitting observations of Bennu's thermal emission acquired at seven different local times of day by two spacecraft-based spectrometers: the OSIRIS-REx Thermal Emission Spectrometer (OTES, Christensen et al., 2018), and the OSIRIS-REx Visible and InfraRed Spectrometer (OVIRS, Reuter et al., 2018). Spatial variations in thermal inertia and surface roughness were originally mapped to the 49,000-facet version of the v34 shape model (Barnouin et al., 2020), which we degraded by spatial averaging to the 12,000-facet version used in this work to improve the computational performance. Thus, the only remaining free parameter in this third model was the bulk density of Bennu.

3.3. Solar radiation pressure and Poynting–Robertson drag

Solar radiation pressure is generally only visible on small objects of several meters in size (MPEC 2008-D12,[9] Micheli et al., 2012, 2013, 2014; Mommert et al., 2014a,b; Farnocchia et al., 2017b; Fedorets et al., 2020). Though Bennu is a half-kilometer-diameter asteroid, given the extreme accuracy required to model its orbit, we included solar radiation pressure using a spherical model as in Vokrouhlický and Milani (2000). Based on the radius of 246 m and the GM of 4.890 m^3/s^2 (Scheeres et al., 2020a; Chesley et al., 2020), the area-to-mass ratio is 2.6×10^{-6} m^2/kg.

Another solar radiation term to be taken into account is the Poynting–Robertson drag, an aberration effect caused by the motion of Bennu relative to the Sun that offsets the direction of the incoming photon from purely radial (Burns et al., 1979; Vokrouhlický and Milani, 2000). Similar to the Yarkovsky effect, the Poynting–Robertson drag also causes a secular drift in semimajor axis, which, for the area-to-mass ratio of Bennu, is about −0.4 m/yr. While this drift is far smaller than that caused by the Yarkovsky effect of −284 m/yr as calculated in Chesley et al. (2014), the effect of the Poynting–Robertson drag is above the level of uncertainty of the Yarkovsky da/dt estimate (see Section 5) and so cannot be neglected.

3.4. Numerics

The JPL Comet and Asteroid Orbit Determination Package employs a variable order Adams integrator called DIVA (Krogh, 1974). Integration in double precision turned out to be insufficiently accurate, so we used a quadruple precision version of the integrator with integration tolerance of 10^{-18}, which we selected upon checking convergence while progressively tightening the tolerance by a factor of 10. The estimate of the Bennu bulk density and the coordinates on the 2135 B-plane were statistically identical for tolerances of 10^{-17}, 10^{-18}, and 10^{-19} with differences within 3×10^{-5} kg/m^3 and 25 m, respectively. These differences point to a numerical error in the integration to 2135 of tens of meters, well below the uncertainties (see Section 4).

4. Orbit determination

We computed an orbit solution by fitting all ground-based optical and radar astrometry and the pseudo-range points derived from OSIRIS-REx tracking. The optical dataset comprises 580 observations from 1999-09-11 to 2018-05-15. We applied the Eggl et al. (2020) star catalog debiasing scheme and the Vereš et al. (2017) weighting scheme, but retained the manual weights and rejections by Chesley et al. (2014). Radar observations collected in 1999, 2005, and 2011 include 22 delay measurements and seven Doppler measurements, which we weighted at the reported uncertainty. As discussed in Section 2, we assumed a 15-ns uncertainty for the 36 pseudo-range points of Table 1.

The orbit solution was obtained by estimating the following parameters:

- Orbital elements at osculating epoch 2011 January 1.0 TDB;
- Bulk density of Bennu, used as a scaling parameter for the Yarkovsky model;
- Area-to-mass ratio of Bennu, which was initially set to 2.6×10^{-6} m^2/kg with an a priori uncertainty of 10%;
- Masses of 343 perturbers, which are given together with the a priori masses and uncertainties in Table A.1;
- A constant delay bias for the pseudo-range points with an a priori uncertainty of 10 ns based on pre-flight calibration of the OSIRIS-REx high-gain antenna delay.

Table 2 gives the Bennu orbit solution and the corresponding formal uncertainties. The reported bulk density and uncertainties are really a measure of the Yarkovsky effect on Bennu and should not be interpreted as a direct bulk density measure. The Yarkovsky model has inherent uncertainties, at least as large as the absolute OTES calibration (1%, Christensen et al., 2018), that limit the validity of the physical interpretation of the estimated bulk density. Even so, the estimated bulk density is consistent with independent OSIRIS-REx measures (Scheeres et al., 2019; Daly et al., 2020), which attests to the accuracy of the Yarkovsky model employed.

The correction to the perturber masses in the ensemble is statistically significant and lowers the χ^2 of the fit by 47. However, there is no particularly high signal for any individual mass, and all masses

[9] https://www.minorplanetcenter.org/mpec/K08/K08D12.html.

Table 2
Orbit solution 118 for Bennu. The heliocentric orbital elements refer to an osculating epoch of 2011 January 1.0 TDB and are in the IAU76 ecliptic frame (Seidelmann, 1977). The error bars correspond to 1-σ formal uncertainties.

Parameter	Value	Uncertainty	Units
Eccentricity (e)	0.2037450762416	6.97×10^{-11}	
Perihelion distance (q)	0.896894400446	2.30×10^{-10}	au
Time of perihelion TDB (t_p)	2010-08-30.6419408727	2.25×10^{-8}	d
Longitude of node (Ω)	2.0608661957	5.56×10^{-8}	deg
Argument of perihelion (ω)	66.2230608408	6.44×10^{-8}	deg
Inclination (i)	6.03494377025	6.86×10^{-9}	deg
Bulk density (ρ)	1191.535	0.892	kg/m^3
Area-to-mass ratio (A/M)	2.636×10^{-6}	0.191×10^{-6}	m^2/kg
Delay bias	0.08	9.97	ns

remain within their a priori distribution. The only noteworthy case is Herculina, for which the fit lowers the mass from 2.0 km^3/s^2 as estimated by Baer and Chesley (2017) to 0.75 ± 0.70 km^3/s^2. Based on a diameter of 222 km from IRAS (Infrared Astronomical Satellite) measurements (Tedesco et al., 2002), the Baer and Chesley (2017) mass estimate would result in a density of 5 g/cm^3. Because Herculina is an S-type asteroid (Bus and Binzel, 2002) a lower mass and a lower density make sense (Carry, 2012).[10] Our estimated mass is consistent with that reported by Carry (2012): 0.8 ± 0.2 km^3/s^2.

Fig. 2 shows the residuals for all the data used in the fit. Compared to solution 85 from Chesley et al. (2014), the inclusion of pseudo-range points result in a 2.2-σ correction. Ground-based radar delay measurements are the most penalized by the correction. Even though they still fit well within the stated uncertainties, the corresponding delay χ^2 increases by 3.8, and the delay residuals show a linear trend in 2005 and a bias in 2011 (see bottom left panel of Fig. 2) that were not present in Chesley et al. (2014). Doppler measurements do not experience any meaningful penalty due to the orbit correction, while the χ^2 of optical data increases by 1.0.

One manifestation of this 2.2-σ orbit correction is in the mapping to the 2135 encounter with Earth. The left panel of Fig. 3 shows the comparison of Öpik's ζ coordinate on the corresponding B-plane (Valsecchi et al., 2003) between the Chesley et al. (2014) solution and the updated one based on OSIRIS-REx data. The uncertainty in ζ_{2135} is now 3769 km, a factor of ~20 smaller than that based on ground-based data alone (Chesley et al., 2014).

For the time frame of the OSIRIS-REx mission, the Bennu trajectory is publicly available[11] and Fig. 4 shows the Bennu position and velocity uncertainties projected into the geocentric plane-of-sky frame and radial–transverse–normal frame. Thanks to the pseudo-range points, the radial distance between Earth and Bennu has an uncertainty of few meters. The other components have uncertainties within a few tens of meters.

The number of estimated parameters may appear excessive and some of them (e.g., some of the perturber masses) do not meaningfully improve the fit to the data. However, these estimates are constrained by an a priori distribution that reflects the a priori knowledge of their values, thus keeping the solution from converging to unrealistic values. Moreover, the inclusion of these parameters allows their uncertainties to contribute to the Bennu ephemeris uncertainties. Fig. 5 shows how the estimates of the Bennu bulk density and ζ_{2135} evolve as the number of estimated perturber masses increases. With the first few tens of perturbers, the estimates experience substantial changes and then converge once about 180 perturber masses are estimated. Also, the uncertainties in bulk density and ζ_{2135} are initially small and progressively increase as more perturber masses are estimated to finally converge. Similarly, there is no significant added knowledge on the delay bias for the pseudo-range points from the fit. However, including this parameter in the fit ensures that the uncertainty of the Bennu ephemeris accounts for the uncertainty of the high-gain antenna calibration. In turn, the Bennu position in geocentric range cannot be known to better than 1.5 m, which corresponds to 10 ns in range. Therefore, the large number of parameters included increases the uncertainties in our solution to more realistic values.

5. Yarkovsky-driven semimajor axis drift

By decomposing the Yarkovsky acceleration in the radial, transverse, and normal components (a_R, a_T, a_N), we can compute the instantaneous change in semimajor axis da/dt using Gauss's planetary equations (Battin, 1987; Bertotti et al., 2003):

$$\frac{da}{dt} = \frac{2}{n\sqrt{1-e^2}} \left(e \sin f a_R + \frac{p}{r} a_T \right) , \quad (1)$$

where r is the heliocentric distance, a is the semimajor axis, e is the eccentricity, f is the true anomaly, $p = a(1-e^2)$ is the semilatus rectum, and n is the mean motion. Fig. 6 shows the da/dt caused by the Yarkovsky effect on Bennu as a function of true anomaly and heliocentric distance for the orbital elements and bulk density of Table 2. The average in time over a Keplerian orbital revolution gives $da/dt = -284.59 \pm 0.21$ m/yr, where the uncertainty reflects that of the estimated bulk density (Table 2). The corresponding signal-to-noise ratio is ~1400. This estimate is 0.5-σ from the Chesley et al. (2014) estimate based on ground-based optical and radar astrometry. Given the small 0.21 m/yr uncertainty in da/dt, neglecting the Poynting–Robertson drag (Section 3.3) would lead to a 2-σ error.

The Yarkovsky semimajor axis drift is not constant over time but is a function of the orbital elements of Bennu. As discussed in Section 3.2, the Yarkovsky acceleration itself depends on the orbital elements, which is why we computed it on a grid of orbital elements to be interpolated. The conversion from acceleration to da/dt (Eq. (1)) also depends on the orbital elements.

Fig. 7 shows the evolution of the Bennu orbital elements and the Yarkovsky-driven da/dt. Close approaches to Earth cause sudden variations in the parameters except for the longitude of ascending node Ω, which only displays a secular trend and is not affected by close approaches because they take place at the node crossing. The variations in da/dt exceed its formal uncertainty, so estimated da/dt is tied to the epoch 2011 January 1.0 TDB and the corresponding orbital elements (Table 2).

6. Impact hazard assessment

The improved knowledge of the future trajectory of Bennu allows us to refine the assessment of the possibility of a future impact on Earth. When mapped to the B-plane corresponding to the Earth encounter in 2135, the uncertainty is only 3769 km (Fig. 3). Therefore, many of the possible impacts identified by Chesley et al. (2014) can now be ruled out. In particular, among the 26 keyholes larger than 1 km, only two persist within the ζ_{2135} distribution. Among the eight keyholes that had an impact probability greater than 10^{-5}, only one (2193) persists.

We first mapped the orbital solution of Table 2 to 2135-09-15, i.e., one week prior to the Earth encounter of 2135. Then, we performed a statistical Monte Carlo impact analysis by generating 10 million samples from the mapped state covariance, propagating each sample through 2300 (100 years beyond the horizon considered by Chesley et al., 2014), and counting the number of impacts. Table 3 lists all the impacts we found with a probability greater than 5×10^{-7}, along with the corresponding keyhole location and width on the 2135 B-plane, and Palermo scale (Chesley et al., 2002). The cumulative impact probability is 5.7×10^{-4} and the cumulative Palermo scale value is -1.42, a modest increase over the pre-OSIRIS-REx assessment of 3.7×10^{-4} (Chesley et al.,

[10] A revision of the Baer and Chesley (2017) mass estimate led to $GM = 1.5$ km^3/s^2 (Baer, personal communication).

[11] ftp://ssd.jpl.nasa.gov/pub/eph/small_bodies/orex/asteroid/sb-101955-118.tsp.

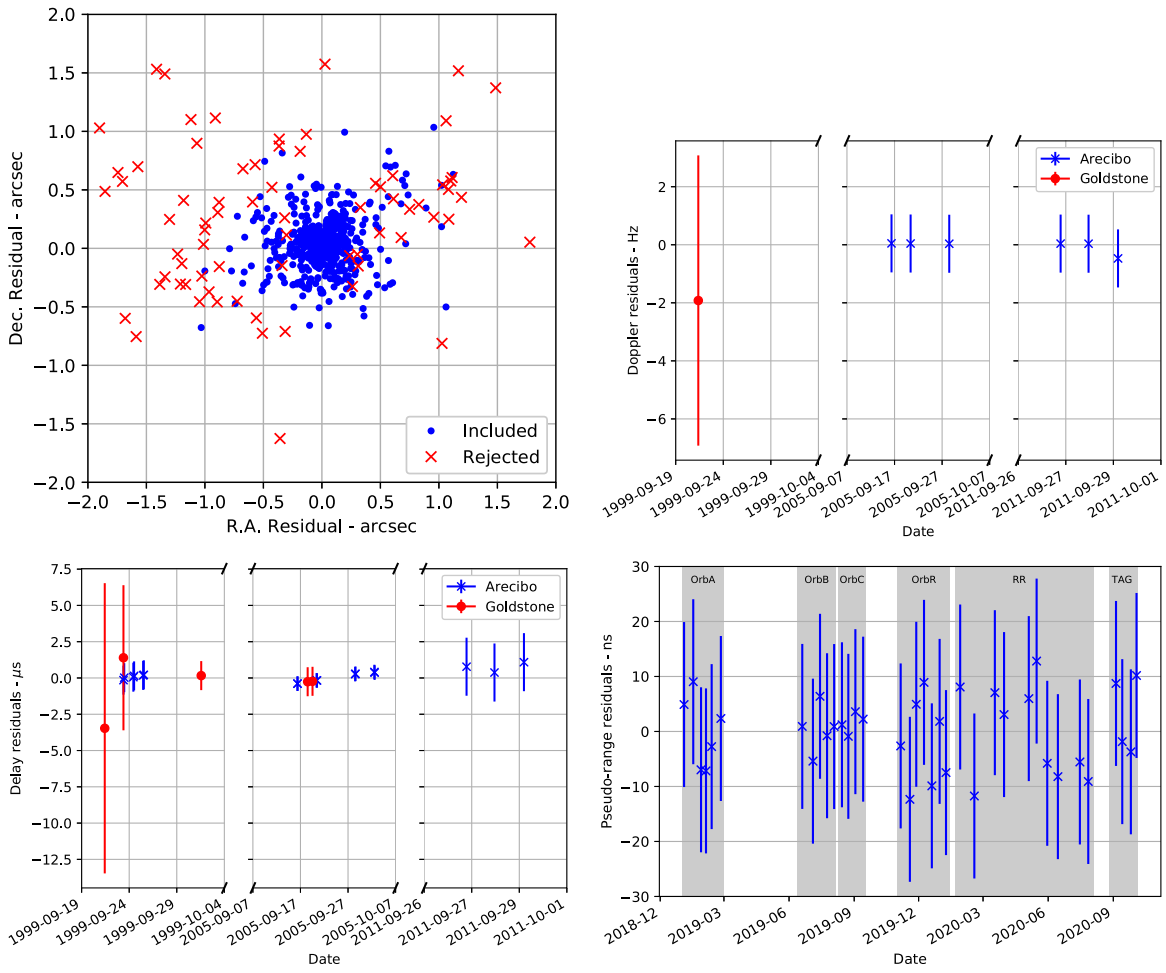

Fig. 2. Residuals of ground-based optical Right Ascension and Declination (top left panel), radar Doppler (top right panel), and radar delay (bottom left panel) measurements, and of pseudo-range points (bottom right panel). For the latter three data types, vertical bars correspond to 1-σ uncertainties. There are 489 optical observations included in the fit and 91 deleted (some of which fall outside of the plot boundaries). The shaded areas in the bottom right panel correspond to the mission phases as in Table 1.

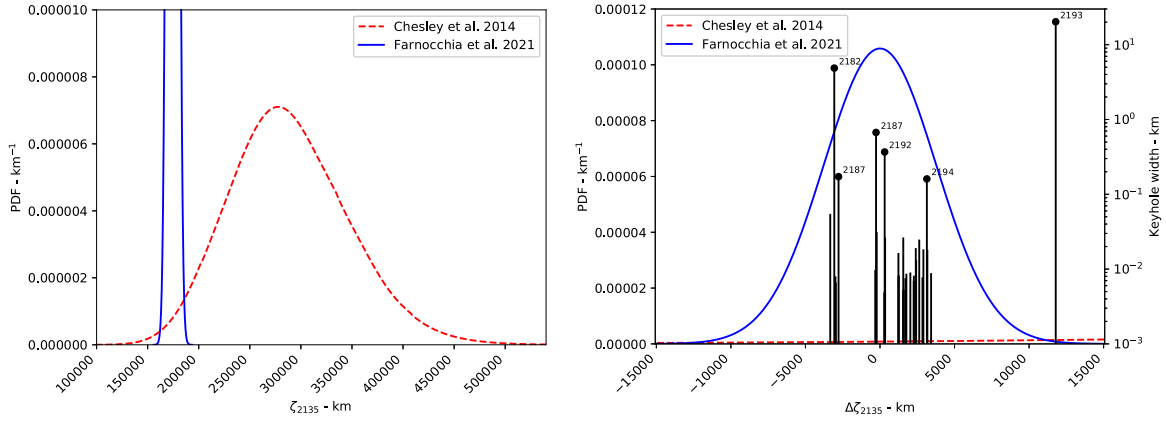

Fig. 3. Probability density function (PDF) of Öpik's ζ coordinate on the B-plane (Valsecchi et al., 2003) of the 2135 encounter with Earth. The left panel compares the Chesley et al. (2014) solution with the one presented in this paper, whose peak is about 10 times the y-axis upper bound because of its 1-σ uncertainty of 3768 km. The right panel is centered at $\zeta_{2135} = 174\,629$ km and compares the updated distribution with the keyholes corresponding to future impacts with a probability of at least 5×10^{-7}. The keyholes wider than 100 m are labeled with the corresponding impact year.

2014). The potential impact in 2182 has the largest individual impact probability and Palermo scale value, 3.7×10^{-4} and -1.60, respectively.

The right panel of Fig. 3 shows the updated keyhole map. In the range covered by the ζ_{2135} distribution, we find all the keyholes greater than 100 m found by (Chesley et al., 2014) (the one for 2199 at $\zeta_{2135} =$ 186 000 km is not shown in Table 3 because the impact probability is 10^{-7}). Moreover, the higher densification of the Monte Carlo samples reveal much smaller keyholes, as small as several meters. This behavior is expected because each encounter can spawn a complicated, possibly fractal, sequence of resonant returns (Valsecchi et al., 2003). Some of the keyhole ζ_{2135} locations are shifted by up to several kilometers relative to their locations as specified by Chesley et al. (2014). The

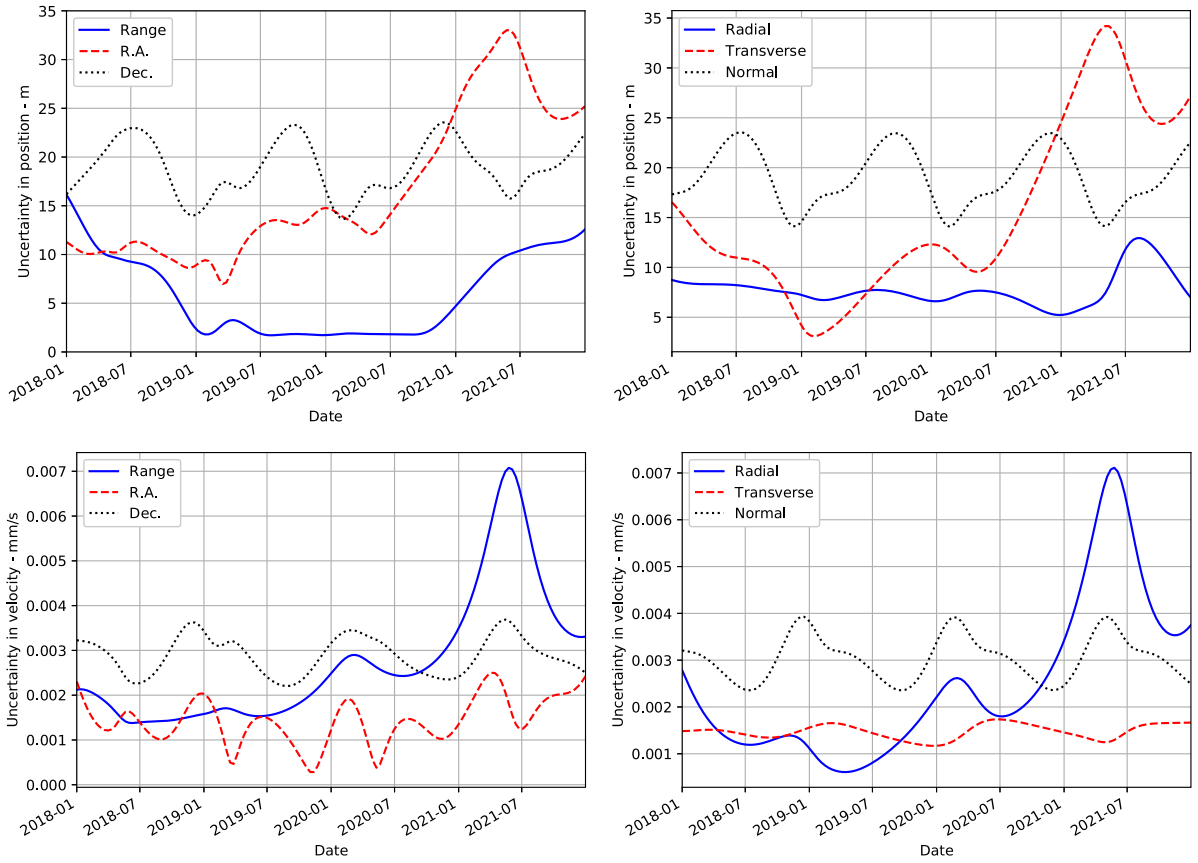

Fig. 4. Formal 1-σ position (top panels) and velocity (bottom panels) uncertainties of Bennu in either the geocentric range, Right Ascension, and Declination directions (left panels) or the radial, transverse, and normal directions (right panels).

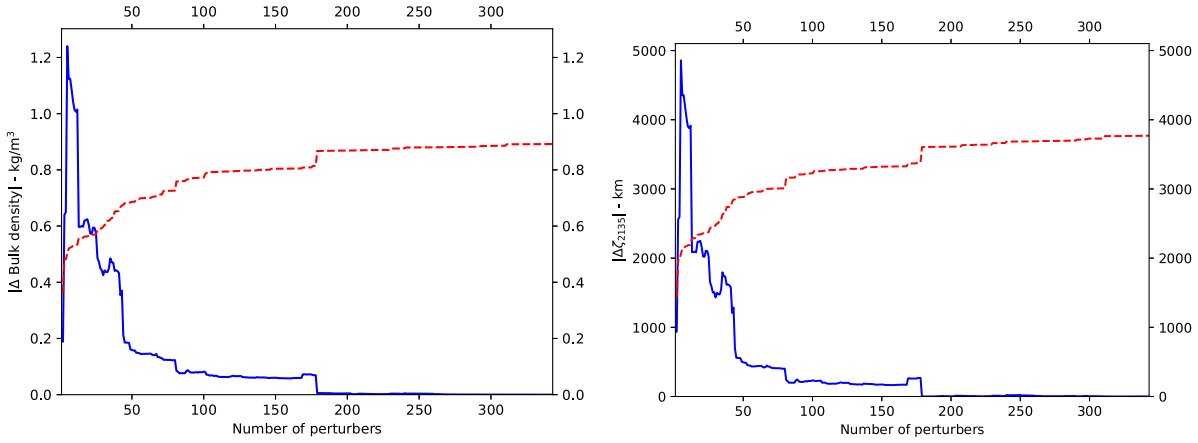

Fig. 5. Absolute variation of bulk density (solid line, left panel), ζ_{2135} (solid line, right panel), and their uncertainties (dashed lines) as a function of the number of perturbers included in the model. The final bulk density and ζ_{2135} estimates are 1191.535 ± 0.892 kg/m^3 and $174\,629 \pm 3769$ km, respectively.

cause is a small (~2 km) shift in ξ_{2135}, which, given the incidence angle between the line of variations and the resonant-return circles (Valsecchi et al., 2003), displaces the keyhole ζ_{2135} locations by several kilometers.

7. Sensitivity of the results to the modeling assumptions

Despite the high-fidelity models employed, it is not possible to capture all the possible sources of errors in the formal uncertainties of the orbital solution (Table 2), the Yarkovsky semimajor axis drift (Section 5), and the assessment of possible future impacts (Section 6). Therefore, we considered model variations to assess the sensitivity of the presented results, summarized in Table 4. Fig. 8 shows the model variations when mapped onto the B-plane of the 2135 encounter with Earth.

7.1. Planetary ephemeris and small-body perturbers

As reference planetary ephemeris we used JPL's DE424 (Folkner, 2011). A planetary ephemeris is a complex model with a large number of estimated parameters, e.g., planet masses and states. Accounting for the resulting uncertainties would significantly complicate the Bennu trajectory estimation problem.

Beyond the sensitivity to the planetary ephemeris, another concern is that of ensuring that no small-body perturber that could significantly

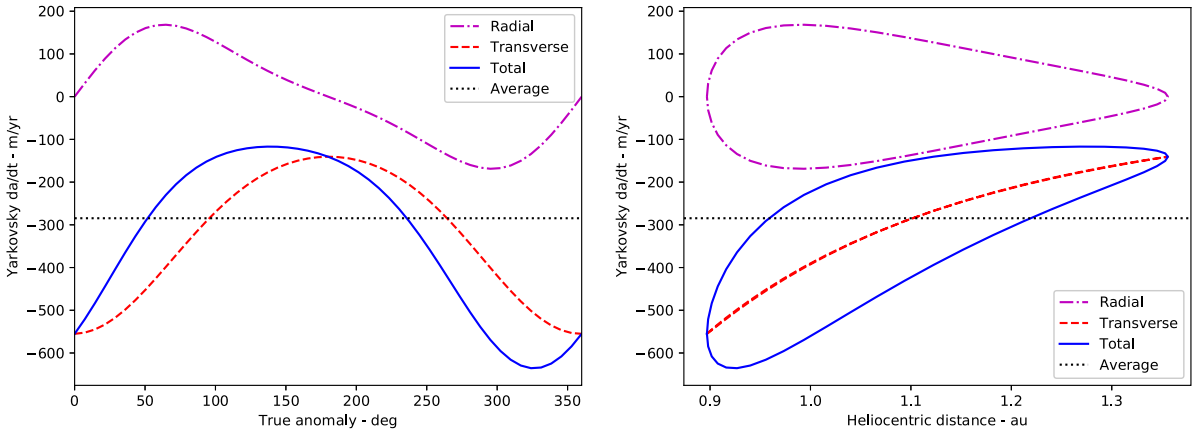

Fig. 6. Yarkovsky-driven semimajor axis drift for Bennu as a function of true anomaly (left panel) and heliocentric distance (right panel). The calculated semimajor axis drift corresponds to the orbital elements and bulk density of Table 2.

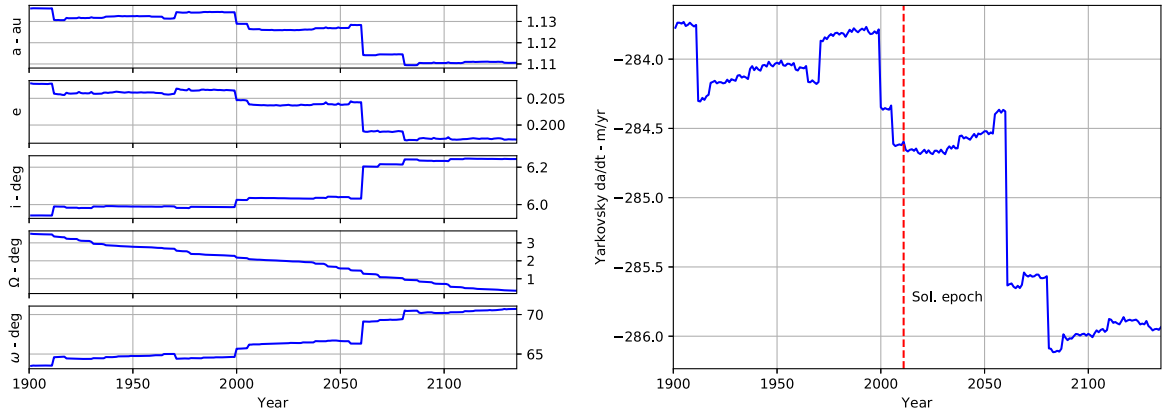

Fig. 7. Evolution of orbital elements (left panel) and Yarkovsky-driven semimajor axis drift (right panel) from 1900 to 2135. Close approaches to Earth in 1911, 1970, 1999, 2005, 2054, 2060, and 2080 (Chesley et al., 2014) cause rapid changes in the orbital elements and in turn in the semimajor axis drift.

Table 3
Impact dates, keyhole centers and widths in the 2135 B-plane, impact probabilities, and Palermo scale values (Chesley et al., 2002). We only show virtual impactors with impact probability $\geq 5 \times 10^{-7}$. Impact probabilities $\geq 10^{-5}$ are in bold. The table is sorted by ζ_{2135}.

Date TDB	ζ_{2135} km	Width km	Impact probability	Palermo scale	Date TDB	ζ_{2135} km	Width km	Impact probability	Palermo scale
2193-09-24.51	171 293	0.053	3.8e−06	−3.61	2185-09-24.55	176 219	0.005	5.0e−07	−4.47
2182-09-24.85	**171 563**	**4.9**	**3.7e−04**	**−1.60**	2189-09-24.50	176 331	0.007	7.0e−07	−4.34
2191-09-24.94	171 640	0.008	6.0e−07	−4.41	2193-09-24.48	176 366	0.005	5.0e−07	−4.49
2196-09-24.21	171 667	0.006	5.0e−07	−4.50	2179-09-25.05	176 398	0.008	8.0e−07	−4.25
2187-09-24.99	**171 849**	**0.17**	**1.4e−05**	**−3.03**	2213-09-25.26	176 665	0.009	8.0e−07	−4.34
2203-09-26.03	174 310	0.009	1.0e−06	−4.22	2181-09-24.50	176 890	0.007	6.0e−07	−4.38
2187-09-25.06	**174 365**	**0.67**	**7.1e−05**	**−2.33**	2187-09-24.97	176 902	0.008	7.0e−07	−4.33
2192-09-24.18	174 409	0.030	3.2e−06	−3.68	2191-09-25.02	177 030	0.019	1.6e−06	−3.98
2208-09-25.25	174 914	0.005	5.0e−07	−4.53	2185-09-24.47	177 055	0.013	1.1e−06	−4.13
2192-09-24.31	**174 943**	**0.37**	**3.9e−05**	**−2.60**	2184-09-24.30	177 262	0.024	2.0e−06	−3.87
2197-09-24.41	174 974	0.026	2.7e−06	−3.77	2195-09-24.99	177 477	0.008	6.0e−07	−4.42
2197-09-24.44	175 865	0.016	1.6e−06	−4.00	2210-09-25.69	177 539	0.018	1.4e−06	−4.09
2192-09-24.18	175 874	0.008	8.0e−07	−4.29	**2194-09-24.78**	**177 773**	**0.16**	**1.2e−05**	**−3.12**
2187-09-24.96	175 881	0.008	8.0e−07	−4.27	2210-09-25.74	177 807	0.018	1.3e−06	−4.12
2195-09-24.92	176 188	0.005	5.0e−07	−4.50	2199-09-25.03	178 057	0.009	6.0e−07	−4.43
2190-09-24.78	176 190	0.026	2.5e−06	−3.79	**2193-09-24.59**	**186 416**	**20**	**1.6e−05**	**−2.99**

affect the motion of Bennu is neglected. The 343 perturbers we included (Table A.1) are expected to represent 90% of the total mass of the main asteroid belt (Folkner et al., 2014). Based on Fig. 5, the orbital solution appears to have converged in terms of both nominal value and uncertainty, which is a good indication that the set of perturbers is sufficient.

We tested the sensitivity of the Bennu trajectory estimate to the planetary ephemeris by switching to the DE440 version (Park et al., 2021). In addition to the 343 perturbers of Table A.1, this ephemeris also includes Trans-Neptunian Objects (TNOs), which we added to the force model to further test the sensitivity to the selected set of perturbers. Although the orbital fit slightly improves ($\Delta\chi^2 = 2$), there is only a 2×10^{-5} relative change in the estimated Yarkovsky drift, which corresponds to a 0.03-σ difference (Table 4). The map onto the B-plane (Fig. 8) is also consistent with the baseline setup. In terms of impact probabilities, among the cases with a probability $\geq 10^{-5}$ results do not change by more than 30%, with the exception of the 2193 keyhole at $\zeta_{2135} = 186\,416$ km, whose probability increases from

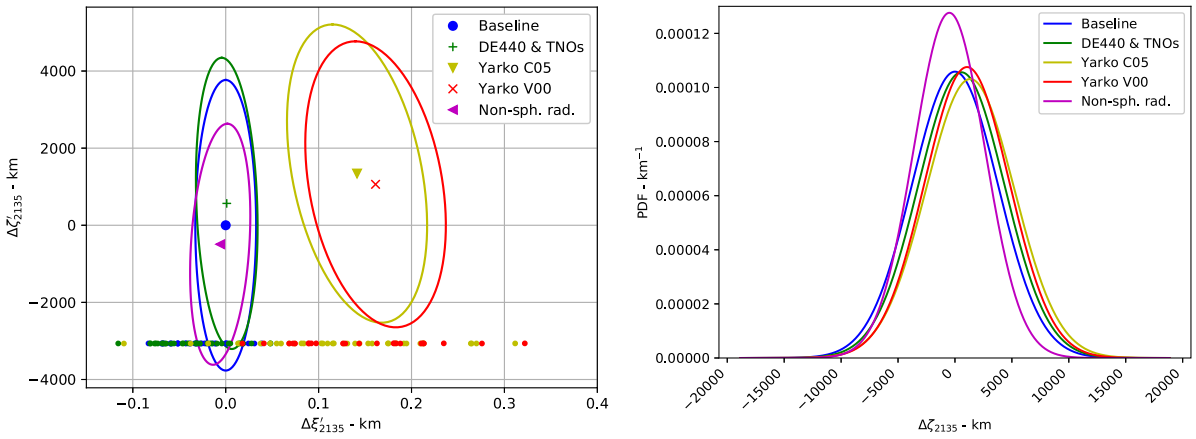

Fig. 8. Mapped uncertainties on the B-plane of the 2135 encounter with Earth for model variations relative to the baseline model (Section 3): different planetary ephemeris and set of small-body perturbers (Section 7.1), different Yarkovsky models (Section 7.2), and non-spherical modeling of solar radiation pressure (Section 7.5). The left panel is centered at $(\xi_{2135}, \zeta_{2135}) = (-125\,327, 174\,629)$ km. The axes are slightly rotated counterclockwise by 0.31° relative to the Öpik frame (Valsecchi et al., 2003) to align with the ellipse axes and obtain an optimal view of the solution differences. Ellipses correspond to the 1-σ level. The dots represent Monte Carlo solutions impacting in 2182 and show that future impacts are determined by ζ_{2135} alone. The right panel shows the probability distributions in ζ_{2135} and is centered at $\zeta_{2135} = 174\,629$ km.

Table 4
Yarkovsky-driven semimajor axis drift and ζ_{2135} for model variations. The formal 1-σ uncertainties in da/dt and ζ_{2135} are 0.21 m/yr and 3769 km, respectively. "Baseline" indicates modeling conditions as described in Section 3. The different model variations indicated in each subsequent row are described in Section 7.

Case	da/dt m/yr	$\Delta da/dt$ m/yr	$\Delta da/dt$ σ	ζ_{2135} km	$\Delta\zeta_{2135}$ km	$\Delta\zeta_{2135}$ σ
Baseline	−284.595	–	–	174 629	–	–
DE440 & TNOs	−284.589	0.006	0.03	175 196	567	0.15
Yarko C05	−284.522	0.073	0.35	175 969	1340	0.36
Yarko V00	−284.517	0.078	0.37	175 691	1062	0.28
Sun's J2	−284.602	−0.008	−0.04	174 688	59	0.02
Non-sph. rad.	−284.549	0.046	0.22	174 136	−493	−0.13
No PR drag	−284.974	−0.379	−1.80	174 636	7	0.002
Galilean satellites	−284.600	−0.005	−0.02	174 689	60	0.016
Solar mass loss	−284.617	−0.022	−0.10	174 643	14	0.004

1.6×10^{-5} to 2.4×10^{-5}. This keyhole is located deep in the tail of the ζ_{2135} probability distribution, which results in higher sensitivity of the impact probability.

7.2. Yarkovsky model

The Rozitis et al. (2020, R20) model discussed in Section 3.2 is the highest-fidelity thermal model currently available for Bennu. However, it has some uncertainty (e.g., OTES calibration) that is hard to capture in our simple parametrization with the bulk density used as a scale factor. The Čapek and Vokrouhlický (2005, C05) and Vokrouhlický et al. (2000, V00) models are not as accurate but are more flexible in that they allow us to estimate thermal inertia along with the bulk density.

Switching the Yarkovsky model does not change the estimated Yarkovsky drift by more than 0.35-σ (Table 4). On the other hand, on the 2135 B-plane, there is a small (about 150 m) but statistically significant offset (about 2-σ) in the ξ_{2135} direction (see left panel of Fig. 8). However, in terms of impact analysis, ζ_{2135} is what defines the keyhole and, in that coordinate, the different models are consistent (right panel of Fig. 8). Among the potential impacts with a probability of at least 10^{-5}, we again see changes within 32% for the keyholes within the core of the distribution. The largest variation is for the 2182 impact probability, which can be as low as 2.5×10^{-4}. The 2193 keyhole at $\zeta_{2135} = 186\,416$ km can have a probability as large as 5.5×10^{-5}.

Another source of error is the uncertainty in the Bennu rotation rate and pole orientation. Changing these parameters in the Rozitis et al. (2020, R20) or Čapek and Vokrouhlický (2005, C05) models would require an intensive calculation. For the purpose of this sensitivity analysis, we used the Vokrouhlický et al. (2000, V00) model and changed the rotation rate by 1%, which caused a 0.02-m/yr difference in da/dt and a 45-km difference in ζ_{2135}. Changing the pole's R.A. and Dec. by 0.01° caused a 0.0004-m/yr change in da/dt and a 13-km difference in ζ_{2135}. These differences are ignorable and even overestimate the actual effect, given that the uncertainty in the spin rate and pole (Hergenrother et al., 2019; Daly et al., 2020) are far smaller than the variations we assumed.

7.3. Solar torque

Because of the Yarkovsky effect's dependence on the rotation pole orientation of Bennu, we considered the influence of solar gravitational torque (e.g., Bertotti et al., 2003, Sec. 4.1). Solar gravity exerts a net torque on a non-spherical orbiting asteroid, which averages out in terms of rotation rate ω_{rot} but produces a secular precession of the pole given by

$$\frac{d\mathbf{s}}{dt} = -\alpha\,(\mathbf{N}\cdot\mathbf{s})\,(\mathbf{N}\times\mathbf{s}) \quad , \quad \alpha = \frac{3}{2}\,\frac{n^2}{\omega_{rot}(1-e^2)^{3/2}}\,\frac{C-(A+B)/2}{C}\,, \tag{2}$$

where $\mathbf{s}$ is the spin pole orientation, $\mathbf{N}$ is the unit vector in the direction of orbital angular momentum, α is the precession constant, n is the mean motion, e the orbital eccentricity, and (A, B, C) the principal values of the inertia tensor of Bennu. From Barnouin et al. (2019) we derived $\alpha \simeq 92.36''$/yr. The resulting average rates of change in R.A. and Dec. over the next 100 years are 0.015°/century and 0.11°/century, respectively. By adding the corresponding polar motion to the Vokrouhlický et al. (2000) (V00) model, the differences relative to the case with a fixed pole are 0.0002 m/yr in da/dt and 4 km in ζ_{2135}, which are ignorable.

7.4. YORP effect

The Yarkovsky–O'Keefe–Radzievskii–Paddack (YORP) effect is closely related to the Yarkovsky effect (Bottke et al., 2006; Vokrouhlický et al., 2015). It consists of a torque on the asteroid caused by the reflected sunlight and its proper thermal radiation, the part also responsible for the Yarkovsky effect. On average, the YORP effect produces secular changes in both the rotation rate and pole orientation of the body. Because the perturbation caused by the Yarkovsky effect depends on the rotation state, the Yarkovsky and YORP effects are typically interconnected in planetary applications. Therefore, it is important to verify to what degree our orbital results could be affected by the existing YORP torques on Bennu.

One aspect of the YORP effect has already been measured for Bennu, namely the acceleration of the rotation rate by about $(3.6 \times 10^{-6})°/d^2$ (Hergenrother et al., 2019). We introduced this rotation acceleration in the Vokrouhlický et al. (2000, V00) model. We found differences relative to the fixed rotation rate case of 0.00001 m/yr in da/dt and 4 km in ζ_{2135}, which can be ignored.

The second component of the YORP effect consists of a tilt in Bennu's rotation pole, which is too small to be directly measured even by the OSIRIS-REx spacecraft. To estimate the magnitude of this change, we can use either theoretical modeling of the YORP effect or a more empirical approach, by assuming a Monte Carlo-generated synthetic torque compatible with the rotation-rate effect. The latter approach may be justified by the fact that YORP modeling strongly depends on small-scale irregularities of the asteroid surface and details of 3D heat conduction through them (e.g., Vokrouhlický et al., 2015). A YORP computation at this level of sophistication has not been developed for Bennu yet. We thus used a much simpler 1D heat conduction model (Čapek and Vokrouhlický, 2004; Čapek and Vokrouhlický, 2005) and the empirical approach mentioned above, which indicated that the YORP-driven change in obliquity of Bennu is less than $0.001°$/century. The reason for the small change is the already high obliquity of Bennu (see Čapek and Vokrouhlický, 2004, for details). The effect on pole precession is larger, but it amounts to less than $\simeq$15% of the regular precession effect due to the solar torque (Section 7.3). Over a century, the total tilt of Bennu's rotation pole due to the YORP effects is smaller than $0.1°$, small enough to be neglected.

7.5. Non-spherical effects in solar radiation accelerations

We considered a solar radiation pressure and Poynting–Robertson drag formulation based on the actual shape of Bennu instead of assuming a spherical shape. In this case we did not estimate the area-to-mass ratio, though the bulk density estimate from the Yarkovsky effect also scaled solar radiation pressure and Poynting–Robertson drag. The difference between this solution and the baseline is compatible with the uncertainties (Table 4 and Fig. 8). Because we did not estimate the area-to-mass ratio independently of the bulk density from the Yarkovsky effect for this model variation, this solution has lower uncertainties that are fully covered by the baseline configuration.

7.6. Oblateness of the Sun, the planets, and the Moon

Our model did not include gravity terms due to the non-spherical shape of the Sun. Table 4 shows that adding the solar J_2 term (with $J_2 = 0.15 \times 10^{-6}$ based on DE424, Folkner, 2011) had a negligible effect on the estimated Yarkovsky semimajor axis drift (0.02 m/yr) and the mapping onto the 2135 B-plane (59 km).

The oblateness of the planets other than Earth is irrelevant. For instance, the Minimum Orbit Intersection Distance (MOID, Gronchi, 2005) between Bennu and Jupiter is 3.9 au and at that distance the Jupiter J_2 acceleration term is $\sim 10^{-49}$ m/s^2. For Mars, the J_2 acceleration at the MOID configuration (0.17 au) is $\sim 10^{-50}$ m/s^2.

The oblateness of the Moon can have a short range effect during a close approach, but can still be ignored. The closest distance between Bennu and the Moon from discovery to 2135 is 0.0044 au in 2060. The corresponding J_2 acceleration term is $< 7 \times 10^{-14}$ m/s^2, which is larger than the Yarkovsky acceleration uncertainty. However, this acceleration decays quickly and thus only matters during the close approach. Conservatively integrating this J_2 acceleration upper bound for two days around the close approach yields a position displacement < 1 mm, well below the Bennu position uncertainties.

Finally, we also quantified the effect of expanding the gravity field for Earth from the default J_2 model to a full 4×4 model (coefficients from Lemoine et al., 1998). The changes in da/dt and ζ_{2135} are 3×10^{-6} m/yr and 0.1 km, respectively, which are ignorable.

7.7. Planetary satellites

In our force model we did not separate the gravitational acceleration of outer planets from that of their satellites, but rather we computed the gravitational acceleration of the corresponding barycenter. This approximation is sufficiently accurate. For instance, by separating the terms from Jupiter and the Galilean satellites using the Lieske (1977) model, we get negligible differences of 0.005 m/yr in da/dt and 60 km in ζ_{2135}. The effect is even smaller for the other outer planets.

7.8. Solar mass loss

Another effect that is not part of our baseline model is the rate of change in solar mass. Therefore, we considered a model variation with the mass of the Sun undergoing a linear relative change of -10^{-13}/yr (Pitjeva et al., 2021) and found ignorable differences: -0.02 m/yr in da/dt and 14 km in ζ_{2135} (Table 4).

7.9. Solar wind

Solar wind represents a highly accelerated flow of plasma, mostly protons and electrons, streaming nearly radially from the Sun. Although solar wind fluctuates in response to the solar variable activity, it can be assessed by its long-term mean values. At low ecliptic latitudes and at 1 au from the Sun (relevant for Bennu's orbit), the radial velocity component of the wind is $w \simeq 400$ km/s and the wind density about 8 protons/cm^3. Similarly to solar radiation, solar wind thus exerts pressure on a moving asteroid. Thanks to its low velocity w compared to the speed of light c, the wind contribution to the radial pressure is very small and may be neglected. However, the drag effect becomes larger because of a larger tilt of the aberration angle and the amplification is roughly c/w. Curiously, solar wind drag generally ranges between 20% and 40% of the Poynting–Robertson drag (Gustafson, 1994; Bertotti et al., 2003), which corresponds to a da/dt value between -0.16 and -0.08 m/yr. Therefore, it is possible that the magnitude of the semimajor axis drift caused by Yarkovsky effect that we measured (Section 5) is overestimated by a comparable amount, which is within the uncertainties.

The impact on the future trajectory is less significant. The future trajectory only depends on the total da/dt, which the fit captures regardless of how that is split between the Yarkovsky acceleration and other perturbations. To prove this point, we considered a model variation where we neglected Poynting–Robertson drag, which leads to an even more significant modeling error. Table 4 shows that the Yarkovsky-related da/dt estimate is off by 2-σ, whereas ζ_{2135} only differs by 7 km, relative to the baseline.

7.10. Ejected particles

The OSIRIS-REx spacecraft observed Bennu ejecting particles of rock from its surface on multiple occasions (Lauretta et al., 2019b; Hergenrother et al., 2020). Scheeres et al. (2020b) analyzed the possibility that these ejection events could affect the orbit evolution of Bennu. They considered a 10-cm particle escaping Bennu in the transverse direction and found that the change in the velocity of Bennu could be at most 0.03% of that caused daily by the Yarkovsky effect. Our uncertainty in the estimated Yarkovsky semimajor axis drift is about 0.07% of its value, so, under the Scheeres et al. (2020b) assumptions, particles could cause a 0.45-σ effect.

However, the above is a worst-case scenario because photometric analysis (Hergenrother et al., 2020) indicated that particle sizes are generally smaller than about 5 cm. Chesley et al. (2020) find that particles greater than 2 cm are rare and that the median particle diameter is 0.7 cm, which reduces the effect by a factor of 1000. Moreover, the largest particle ejection events observed in early 2019 occurred on roughly two-week intervals (Lauretta et al., 2019b), which

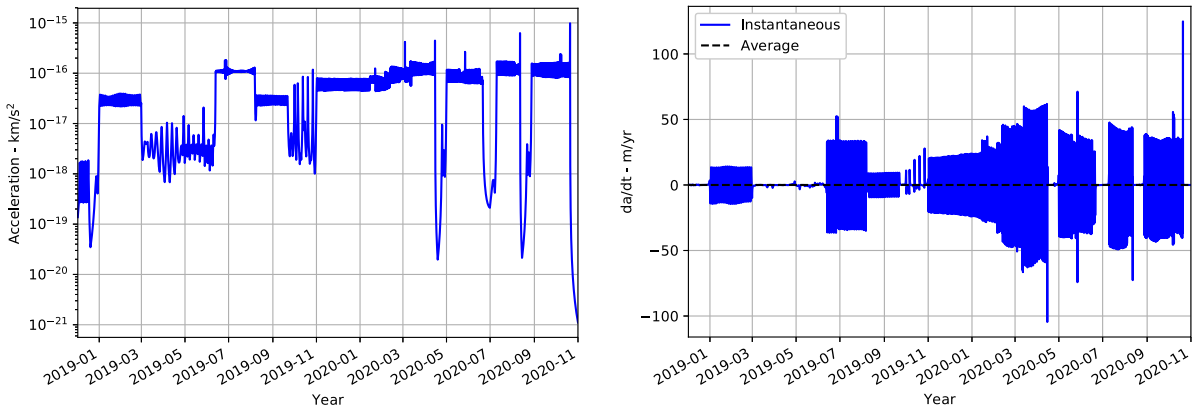

Fig. 9. Gravitational acceleration of the OSIRIS-REx spacecraft on Bennu (left panel) and resulting semimajor axis drift (right panel). The spacecraft mass was set to 1400 kg.

further reduces the overall effect on the Bennu trajectory relative to a daily cadence. For these reasons, it appears extremely unlikely that particle events could significantly affect our Yarkovsky estimate and the trajectory of Bennu.

7.11. Meteoroid impacts

Meteoroid impacts can cause a semimajor axis drift on an asteroid's orbit (Wiegert, 2015). This effect is generally much smaller than that due to the Yarkovsky effect. However, with an uncertainty of only 0.2 m/yr, meteoroid impacts are worth assessing. Using Eq. 3 from Wiegert (2015), the semimajor axis drift caused by meteoroid impacts for an object with the size and bulk density of Bennu, at 1 au from the Sun, is $da/dt \sim -0.01$ m/yr, which is small enough to be ignored.

7.12. Interaction with the OSIRIS-REx spacecraft

Given the level of precision of these analyses, the interaction between Bennu and the OSIRIS-REx spacecraft could be significant. At launch, the OSIRIS-REx spacecraft had a total wet mass of 2105 kg, which decreased to about 1400 kg by the beginning of proximity operations due to deep space and asteroid approach maneuvers (Lauretta et al., 2017). The left panel of Fig. 9 shows the gravitational acceleration on Bennu caused by the OSIRIS-REx spacecraft. Although this acceleration is smaller than that from the Yarkovsky effect (Fig. 1), it can cause instantaneous semimajor axis drifts that exceed the Yarkovsky uncertainty of 0.2 m/yr (right panel of Fig. 9). However, what really matters is the integrated effect. During survey and reconnaissance phases of the mission, the OSIRIS-REx spacecraft spent limited time in the proximity of Bennu during flybys. On the other hand, during orbit phases, the net integrated effect of the spacecraft gravitational pull tended to average to zero. Across proximity operations, we obtain a net average da/dt of about 0.001 m/yr, which is far below the uncertainty in the Yarkovsky-driven semimajor axis drift.

A second aspect to be considered is the change in linear momentum imparted by the OSIRIS-REx spacecraft to Bennu as part of the sample collection sequence. Based on Ballouz (2017), a reasonable expectation for the average force on Bennu as a result of TAG is 50 N applied for 5 s. Given the mass of Bennu, the resulting change in the velocity of Bennu is $\simeq 3.4 \times 10^{-9}$ m/s, which is far smaller than the Bennu velocity uncertainties (Fig. 4) and can thus be ignored.

8. Conclusions

The OSIRIS-REx mission to asteroid Bennu has provided exceptional data for testing and improving the accuracy of asteroid trajectory models. During about two years of proximity operations, radiometric ranging to the spacecraft put meter-level constraints on the distance between Earth and Bennu. To be able to match the data, we employed a high-fidelity force model based on JPL planetary ephemeris DE424 (Folkner, 2011) that included perturbations from 343 small-body perturbers and relativistic effects from the Sun, the planets, Pluto, and the Moon. The masses of the 343 perturbers were estimated to be able to fit the data. Nongravitational perturbations included the Yarkovsky effect, solar radiation pressure, and Poynting–Robertson drag. In addition, we used a quadruple precision integrator because the double precision integrator was insufficiently accurate to match the ranging data.

We modeled the Yarkovsky perturbation using a thermophysical model based on characterizations by OSIRIS-REx in proximity (Rozitis et al., 2020), whose only free parameter was the bulk density of Bennu. The bulk density as estimated from the fit to the data is within 0.1% of that estimated independently from gravity analysis and shape modeling (Scheeres et al., 2020a; Daly et al., 2020). This level of consistency attests to the accuracy of the Rozitis et al. (2020) Yarkovsky model.

We measured a Yarkovsky-related semimajor axis drift $da/dt = -284.6 \pm 0.2$ m/yr, corresponding to a signal-to-noise ratio of 1400. This value of the drift refers to the osculating elements on 2011 January 1. As the orbit of Bennu evolves due to Earth encounters and planetary perturbations, da/dt varies between -284 m/yr and -286 m/yr from 1900 to 2135. Given the small uncertainty in da/dt, accounting for the Poynting–Robertson drag is important to avoid biasing the estimate. We ascertained the robustness of the da/dt estimate by checking its sensitivity to the specific planetary ephemeris used, the specific Yarkovsky model, rotation state uncertainties, solar torque, YORP effect, oblateness of the Sun, planets, and the Moon, separation between outer planets and their moons, solar mass loss, non-spherical terms in solar radiation pressure and Poynting–Robertson drag, particle ejections, meteoroid impacts, and interactions with the OSIRIS-REx spacecraft. Solar wind drag is the largest source of modeling error and can reduce the magnitude of the estimated da/dt from the Yarkovsky effect by up to 0.16 m/yr.

The improved orbital knowledge allowed us to refine the impact hazard assessment, which we extended through 2300. The dense structure of keyholes on the B-plane of the 2135 encounter with Earth (Chesley et al., 2014) made it unlikely to avoid all possible pathways to impact. Still, the uncertainties for the 2135 encounter decreased by a factor of about 20, and so many of the most significant impacts found by Chesley et al. (2014) are now ruled out. The cumulative impact probability is 5.7×10^{-4} and the Palermo scale value is -1.42, making Bennu the highest-ranked body in terms of Palermo scale, tied with (29075) 1950 DA (Farnocchia and Chesley, 2014).[12] The highest

[12] https://cneos.jpl.nasa.gov/sentry/.

individual impact probability is 3.7×10^{-4} for September 2182, corresponding to a Palermo scale value of −1.60. The 2037 close approach to Earth represents the next opportunity to collect radar data and therefore to test the accuracy of the ephemeris prediction and further improve the assessment of possible collisions with Earth.

Data availability

All OSIRIS-REx data are archived in the Small Bodies Node of the Planetary Data System at https://sbn.psi.edu/pds/resource/orex/. Shape models of Bennu are available via the Small Body Mapping Tool (http://sbmt.jhuapl.edu/). Kernels and small-force files are available via NASA's Navigation and Ancillary Information Facility (https://naif.jpl.nasa.gov/pub/naif/ORX/; Acton (1996), Acton et al. (2018).

Acknowledgments

We thank C. Wolner for her assistance in preparing the manuscript, J. Baer for revisiting the estimate of the mass of Herculina, and W. Folkner and A. Konopliv for useful discussions. We are grateful to the entire OSIRIS-REx Team for making the encounter with Bennu possible. Part of the research was carried out at the Jet Propulsion Laboratory, California Institute of Technology, under a contract with the National Aeronautics and Space Administration, USA (80NM0018D0004). This material is based upon work supported by NASA under Contract NNM10AA11C issued through the New Frontiers Program. BR acknowledges funding support from the UK Science and Technology Facilities Council (STFC), UK. The work of DV was partly supported by the Czech Science Foundation, Czech Republic through grant 21-11058S.

Appendix A. Perturber masses

See Table A.1.

Table A.1
A priori and a posteriori perturber masses in km^3/s^2. Uncertainties are 1-σ. The superscripts indicate the reference for the a prior mass estimate: *a* is for Park et al. (2016), *b* for Konopliv et al. (2014), *c* for Baer and Chesley (2017), *d* for Carry (2012), and *e* for Yeomans et al. (2000). All the other masses are taken from JPL planetary ephemeris DE431 (Folkner et al., 2014) and are assumed to have a 100% uncertainty. Ceres, Pallas, and Eros have small uncertainties from spacecraft visits and so the notation is compact: numbers in parentheses indicate the uncertainty of the corresponding digits in the mass value.

Asteroid	A priori mass	A posteriori mass	Asteroid	A priori mass	A posteriori mass
1 Ceres	62.62838(87)[a]	62.62838(87)	4 Vesta	17.288245(12)[b]	17.288245(12)
2 Pallas	13.61 ± 0.33[cd]	13.61 ± 0.32	10 Hygiea	5.47 ± 0.10[cd]	5.47 ± 0.10
704 Interamnia	2.50 ± 0.50[cd]	2.49 ± 0.50	511 Davida	2.40 ± 0.14[cd]	2.40 ± 0.14
15 Eunomia	2.07 ± 0.10[cd]	2.07 ± 0.10	532 Herculina	2.00 ± 1.00[cd]	0.75 ± 0.71
3 Juno	2.00 ± 0.20[cd]	1.98 ± 0.20	52 Europa	1.94 ± 0.10[cd]	1.94 ± 0.10
16 Psyche	1.53 ± 0.10[cd]	1.53 ± 0.10	7 Iris	1.10 ± 0.10[cd]	1.09 ± 0.10
48 Doris	1.00 ± 1.00[d]	0.63 ± 0.96	87 Sylvia	1.00 ± 0.20[d]	1.00 ± 0.20
31 Euphrosyne	1.00 ± 1.00[d]	0.78 ± 0.95	65 Cybele	0.99 ± 0.12[cd]	0.99 ± 0.12
29 Amphitrite	0.94 ± 0.10[cd]	0.94 ± 0.10	88 Thisbe	0.92 ± 0.11[cd]	0.92 ± 0.11
6 Hebe	0.83 ± 0.10[cd]	0.83 ± 0.10	324 Bamberga	0.80 ± 0.20[cd]	0.80 ± 0.20
409 Aspasia	0.80 ± 0.30[d]	0.80 ± 0.30	107 Camilla	0.75 ± 0.10[d]	0.75 ± 0.10
451 Patientia	0.75 ± 0.50[d]	0.65 ± 0.49	372 Palma	0.70 ± 0.50[d]	0.65 ± 0.50
444 Gyptis	0.70 ± 0.20[d]	0.69 ± 0.20	8 Flora	0.67 ± 0.10[cd]	0.67 ± 0.10
13 Egeria	0.65 ± 0.30[d]	0.68 ± 0.30	19 Fortuna	0.65 ± 0.10[cd]	0.65 ± 0.10
154 Bertha	0.60 ± 0.60[d]	0.58 ± 0.59	423 Diotima	0.56 ± 0.30[d]	0.56 ± 0.30
386 Siegena	0.54 ± 0.11[d]	0.54 ± 0.11	22 Kalliope	0.53 ± 0.10[d]	0.53 ± 0.10
259 Aletheia	0.52 ± 0.10[d]	0.52 ± 0.10	9 Metis	0.51 ± 0.10[cd]	0.51 ± 0.10
354 Eleonora	0.50 ± 0.20[d]	0.49 ± 0.20	96 Aegle	0.50 ± 0.50[d]	0.58 ± 0.49
165 Loreley	0.50 ± 0.50[d]	0.54 ± 0.47	536 Merapi	0.50 ± 0.50[d]	0.49 ± 0.50
14 Irene	0.50 ± 0.50[d]	0.52 ± 0.49	185 Eunike	0.50 ± 0.50[d]	0.40 ± 0.49
120 Lachesis	0.50 ± 0.50	0.55 ± 0.49	94 Aurora	0.50 ± 0.50[d]	0.49 ± 0.49
566 Stereoskopia	0.50 ± 0.50	0.49 ± 0.49	39 Laetitia	0.47 ± 0.20[cd]	0.48 ± 0.20
130 Elektra	0.45 ± 0.10[d]	0.45 ± 0.10	89 Julia	0.45 ± 0.30[d]	0.43 ± 0.30
41 Daphne	0.42 ± 0.10[d]	0.41 ± 0.10	117 Lomia	0.41 ± 0.10[d]	0.41 ± 0.10
490 Veritas	0.40 ± 0.25[d]	0.39 ± 0.25	137 Meliboea	0.40 ± 0.40[d]	0.40 ± 0.40
471 Papagena	0.40 ± 0.40[d]	0.49 ± 0.39	128 Nemesis	0.40 ± 0.20[d]	0.40 ± 0.20
702 Alauda	0.40 ± 0.40[d]	0.42 ± 0.40	85 Io	0.40 ± 0.40[d]	0.30 ± 0.39
481 Emita	0.40 ± 0.20[d]	0.41 ± 0.20	24 Themis	0.39 ± 0.20[d]	0.37 ± 0.20
45 Eugenia	0.39 ± 0.10[d]	0.40 ± 0.10	69 Hesperia	0.39 ± 0.10[d]	0.39 ± 0.10
11 Parthenope	0.39 ± 0.05[cd]	0.39 ± 0.05	139 Juewa	0.37 ± 0.20[d]	0.39 ± 0.20
20 Massalia	0.36 ± 0.10[cd]	0.36 ± 0.10	121 Hermione	0.35 ± 0.10[cd]	0.35 ± 0.10
144 Vibilia	0.35 ± 0.10[d]	0.35 ± 0.10	238 Hypatia	0.33 ± 0.11[d]	0.33 ± 0.11
491 Carina	0.32 ± 0.20[d]	0.30 ± 0.20	216 Kleopatra	0.31 ± 0.10[d]	0.31 ± 0.10
56 Melete	0.30 ± 0.10[d]	0.29 ± 0.10	790 Pretoria	0.30 ± 0.10[d]	0.30 ± 0.10
308 Polyxo	0.30 ± 0.30	0.31 ± 0.29	76 Freia	0.30 ± 0.11[cd]	0.30 ± 0.11
469 Argentina	0.30 ± 0.15[d]	0.29 ± 0.15	92 Undina	0.30 ± 0.10[d]	0.30 ± 0.10
747 Winchester	0.30 ± 0.30[d]	0.31 ± 0.29	70 Panopaea	0.29 ± 0.13[d]	0.30 ± 0.13
27 Euterpe	0.26 ± 0.09[cd]	0.27 ± 0.09	168 Sibylla	0.26 ± 0.15[d]	0.26 ± 0.15
349 Dembowska	0.25 ± 0.10[d]	0.25 ± 0.10	804 Hispania	0.25 ± 0.08[cd]	0.25 ± 0.08
106 Dione	0.25 ± 0.25[d]	0.26 ± 0.25	489 Comacina	0.25 ± 0.25	0.27 ± 0.25
712 Boliviana	0.25 ± 0.25	0.21 ± 0.25	268 Adorea	0.25 ± 0.25[d]	0.26 ± 0.25
51 Nemausa	0.25 ± 0.08[cd]	0.25 ± 0.08	196 Philomela	0.25 ± 0.15[d]	0.25 ± 0.15
54 Alexandra	0.25 ± 0.25[d]	0.27 ± 0.25	47 Aglaja	0.25 ± 0.25[d]	0.24 ± 0.25
93 Minerva	0.23 ± 0.10[d]	0.23 ± 0.10	751 Faina	0.22 ± 0.08[d]	0.22 ± 0.08
127 Johanna	0.21 ± 0.10[d]	0.21 ± 0.10	328 Gudrun	0.21 ± 0.10[d]	0.21 ± 0.10
18 Melpomene	0.21 ± 0.10[d]	0.23 ± 0.10	187 Lamberta	0.20 ± 0.20[d]	0.17 ± 0.19
147 Protogeneia	0.20 ± 0.20[d]	0.22 ± 0.20	225 Henrietta	0.20 ± 0.20	0.21 ± 0.20

(*continued on next page*)

Table A.1 (*continued*).

Asteroid	A priori mass	A posteriori mass	Asteroid	A priori mass	A posteriori mass
104 Klymene	0.20 ± 0.20	0.20 ± 0.20	420 Bertholda	0.20 ± 0.20^{d}	0.20 ± 0.20
508 Princetonia	0.20 ± 0.10^{d}	0.20 ± 0.10	164 Eva	0.20 ± 0.20^{d}	0.19 ± 0.20
814 Tauris	0.20 ± 0.20	0.19 ± 0.20	618 Elfriede	0.20 ± 0.20	0.22 ± 0.20
375 Ursula	0.20 ± 0.20^{d}	0.22 ± 0.20	690 Wratislavia	0.20 ± 0.20^{d}	0.20 ± 0.20
129 Antigone	0.20 ± 0.20^{d}	0.17 ± 0.20	59 Elpis	0.20 ± 0.10^{d}	0.19 ± 0.10
5 Astraea	0.18 ± 0.05^{d}	0.18 ± 0.05	146 Lucina	0.18 ± 0.18	0.19 ± 0.18
173 Ino	0.18 ± 0.18^{d}	0.19 ± 0.18	194 Prokne	0.18 ± 0.05^{d}	0.18 ± 0.05
57 Mnemosyne	0.17 ± 0.17^{d}	0.16 ± 0.17	28 Bellona	0.17 ± 0.10^{d}	0.17 ± 0.10
488 Kreusa	0.17 ± 0.10^{d}	0.16 ± 0.10	141 Lumen	0.17 ± 0.17^{d}	0.16 ± 0.17
895 Helio	0.17 ± 0.17^{d}	0.16 ± 0.17	596 Scheila	0.17 ± 0.17	0.16 ± 0.17
212 Medea	0.17 ± 0.17^{d}	0.18 ± 0.17	410 Chloris	0.16 ± 0.16^{d}	0.21 ± 0.16
381 Myrrha	0.16 ± 0.16^{d}	0.16 ± 0.16	12 Victoria	0.16 ± 0.10^{d}	0.16 ± 0.10
74 Galatea	0.16 ± 0.16^{d}	0.18 ± 0.16	334 Chicago	0.15 ± 0.15^{d}	0.15 ± 0.15
46 Hestia	0.15 ± 0.15^{d}	0.16 ± 0.15	134 Sophrosyne	0.15 ± 0.15	0.14 ± 0.15
360 Carlova	0.15 ± 0.15	0.15 ± 0.15	909 Ulla	0.15 ± 0.15	0.15 ± 0.15
388 Charybdis	0.15 ± 0.15	0.14 ± 0.15	68 Leto	0.15 ± 0.15^{d}	0.15 ± 0.15
505 Cava	0.15 ± 0.15^{d}	0.14 ± 0.15	145 Adeona	0.14 ± 0.10^{d}	0.14 ± 0.10
211 Isolda	0.14 ± 0.14^{d}	0.13 ± 0.14	776 Berbericia	0.14 ± 0.14^{d}	0.14 ± 0.14
140 Siwa	0.14 ± 0.14	0.14 ± 0.14	175 Andromache	0.13 ± 0.13	0.13 ± 0.13
705 Erminia	0.13 ± 0.13	0.14 ± 0.13	1093 Freda	0.13 ± 0.13	0.12 ± 0.13
303 Josephina	0.13 ± 0.13	0.13 ± 0.13	159 Aemilia	0.13 ± 0.13	0.12 ± 0.13
230 Athamantis	0.13 ± 0.03^{d}	0.13 ± 0.03	514 Armida	0.13 ± 0.13	0.14 ± 0.13
34 Circe	0.13 ± 0.13^{d}	0.14 ± 0.13	40 Harmonia	0.13 ± 0.13	0.12 ± 0.13
241 Germania	0.13 ± 0.13^{d}	0.13 ± 0.13	387 Aquitania	0.13 ± 0.08^{d}	0.13 ± 0.08
23 Thalia	0.13 ± 0.03^{d}	0.13 ± 0.03	111 Ate	0.12 ± 0.06^{d}	0.12 ± 0.06
30 Urania	0.12 ± 0.06^{d}	0.12 ± 0.06	192 Nausikaa	0.12 ± 0.05^{d}	0.12 ± 0.05
476 Hedwig	0.12 ± 0.05^{c}	0.12 ± 0.05	156 Xanthippe	0.12 ± 0.12^{d}	0.13 ± 0.12
356 Liguria	0.12 ± 0.12^{d}	0.12 ± 0.12	209 Dido	0.12 ± 0.12^{d}	0.12 ± 0.12
95 Arethusa	0.12 ± 0.12	0.12 ± 0.12	466 Tisiphone	0.12 ± 0.12	0.11 ± 0.12
247 Eukrate	0.12 ± 0.12	0.12 ± 0.12	419 Aurelia	0.11 ± 0.05^{d}	0.11 ± 0.05
42 Isis	0.11 ± 0.05^{d}	0.11 ± 0.05	91 Aegina	0.11 ± 0.11	0.12 ± 0.11
162 Laurentia	0.11 ± 0.11	0.11 ± 0.11	35 Leukothea	0.11 ± 0.11	0.11 ± 0.11
772 Tanete	0.11 ± 0.11	0.11 ± 0.11	21 Lutetia	0.11 ± 0.01^{d}	0.11 ± 0.01
105 Artemis	0.10 ± 0.05^{d}	0.10 ± 0.05	654 Zelinda	0.10 ± 0.03^{d}	0.10 ± 0.03
63 Ausonia	0.10 ± 0.05^{d}	0.10 ± 0.05	788 Hohensteina	0.10 ± 0.10	0.10 ± 0.10
37 Fides	0.10 ± 0.10	0.11 ± 0.10	346 Hermentaria	0.10 ± 0.10^{d}	0.10 ± 0.10
595 Polyxena	0.10 ± 0.10	0.10 ± 0.10	602 Marianna	0.10 ± 0.10^{d}	0.10 ± 0.10
86 Semele	0.10 ± 0.10	0.10 ± 0.10	426 Hippo	0.10 ± 0.10	0.10 ± 0.10
276 Adelheid	0.10 ± 0.10	0.10 ± 0.10	344 Desiderata	0.10 ± 0.05^{d}	0.10 ± 0.05
150 Nuwa	0.10 ± 0.10^{d}	0.10 ± 0.10	405 Thia	0.10 ± 0.05^{d}	0.11 ± 0.05
762 Pulcova	0.09 ± 0.03^{d}	0.09 ± 0.03	283 Emma	0.09 ± 0.05^{d}	0.09 ± 0.05
773 Irmintraud	0.09 ± 0.09	0.09 ± 0.09	545 Messalina	0.09 ± 0.09	0.09 ± 0.09
233 Asterope	0.09 ± 0.09	0.09 ± 0.09	250 Bettina	0.09 ± 0.09	0.09 ± 0.09
506 Marion	0.09 ± 0.09	0.09 ± 0.09	769 Tatjana	0.09 ± 0.09^{d}	0.09 ± 0.09
97 Klotho	0.09 ± 0.03^{d}	0.09 ± 0.03	114 Kassandra	0.08 ± 0.08	0.08 ± 0.08
635 Vundtia	0.08 ± 0.08	0.08 ± 0.08	36 Atalante	0.08 ± 0.08^{d}	0.08 ± 0.08
181 Eucharis	0.08 ± 0.08	0.08 ± 0.08	78 Diana	0.08 ± 0.04^{d}	0.08 ± 0.04
191 Kolga	0.08 ± 0.08	0.08 ± 0.08	200 Dynamene	0.08 ± 0.08^{d}	0.08 ± 0.08
203 Pompeja	0.08 ± 0.08	0.08 ± 0.08	275 Sapientia	0.08 ± 0.08	0.08 ± 0.08
221 Eos	0.08 ± 0.08^{d}	0.08 ± 0.08	266 Aline	0.08 ± 0.08^{d}	0.08 ± 0.08
521 Brixia	0.08 ± 0.08	0.08 ± 0.08	357 Ninina	0.08 ± 0.08	0.08 ± 0.08
135 Hertha	0.08 ± 0.04^{d}	0.08 ± 0.04	326 Tamara	0.08 ± 0.08	0.06 ± 0.08
455 Bruchsalia	0.08 ± 0.05^{d}	0.08 ± 0.05	176 Iduna	0.07 ± 0.07	0.07 ± 0.07
626 Notburga	0.07 ± 0.07^{d}	0.07 ± 0.07	148 Gallia	0.07 ± 0.07^{d}	0.07 ± 0.07
26 Proserpina	0.07 ± 0.07^{d}	0.07 ± 0.07	50 Virginia	0.07 ± 0.07^{d}	0.07 ± 0.07
784 Pickeringia	0.07 ± 0.07^{d}	0.07 ± 0.07	335 Roberta	0.07 ± 0.07	0.06 ± 0.07
412 Elisabetha	0.07 ± 0.07	0.07 ± 0.07	780 Armenia	0.07 ± 0.07	0.07 ± 0.07
404 Arsinoe	0.07 ± 0.07^{d}	0.07 ± 0.07	694 Ekard	0.07 ± 0.07	0.07 ± 0.07
171 Ophelia	0.07 ± 0.07	0.07 ± 0.07	980 Anacostia	0.07 ± 0.07	0.07 ± 0.07
709 Fringilla	0.07 ± 0.07	0.07 ± 0.07	393 Lampetia	0.07 ± 0.07	0.06 ± 0.07
407 Arachne	0.07 ± 0.07	0.07 ± 0.07	786 Bredichina	0.07 ± 0.07^{d}	0.07 ± 0.07
675 Ludmilla	0.07 ± 0.07^{d}	0.07 ± 0.07	416 Vaticana	0.07 ± 0.07^{d}	0.07 ± 0.07
1015 Christa	0.06 ± 0.06^{d}	0.06 ± 0.06	102 Miriam	0.06 ± 0.06	0.06 ± 0.06
38 Leda	0.06 ± 0.06^{d}	0.06 ± 0.06	449 Hamburga	0.06 ± 0.06^{d}	0.05 ± 0.06
498 Tokio	0.06 ± 0.06	0.06 ± 0.06	210 Isabella	0.06 ± 0.06^{d}	0.06 ± 0.06
223 Rosa	0.06 ± 0.06	0.06 ± 0.06	110 Lydia	0.06 ± 0.06	0.06 ± 0.06
100 Hekate	0.06 ± 0.06	0.06 ± 0.06	373 Melusina	0.06 ± 0.06	0.06 ± 0.06
17 Thetis	0.06 ± 0.03^{cd}	0.06 ± 0.03	713 Luscinia	0.06 ± 0.06	0.06 ± 0.06
71 Niobe	0.06 ± 0.06	0.06 ± 0.06	674 Rachele	0.06 ± 0.06	0.06 ± 0.06
377 Campania	0.06 ± 0.06	0.06 ± 0.06	350 Ornamenta	0.06 ± 0.06	0.06 ± 0.06
84 Klio	0.06 ± 0.06^{d}	0.06 ± 0.06	90 Antiope	0.06 ± 0.03^{d}	0.06 ± 0.03
345 Tercidina	0.06 ± 0.06^{d}	0.06 ± 0.06	201 Penelope	0.05 ± 0.05	0.05 ± 0.05
240 Vanadis	0.05 ± 0.05^{d}	0.05 ± 0.05	1467 Mashona	0.05 ± 0.05	0.05 ± 0.05
445 Edna	0.05 ± 0.05^{d}	0.05 ± 0.05	366 Vincentina	0.05 ± 0.05	0.05 ± 0.05
313 Chaldaea	0.05 ± 0.05	0.05 ± 0.05	80 Sappho	0.05 ± 0.05	0.05 ± 0.05

(*continued on next page*)

Table A.1 (*continued*).

Asteroid	A priori mass	A posteriori mass	Asteroid	A priori mass	A posteriori mass
696 Leonora	0.05 ± 0.05	0.05 ± 0.05	503 Evelyn	0.05 ± 0.05^d	0.05 ± 0.05
143 Adria	0.05 ± 0.05	0.05 ± 0.05	236 Honoria	0.05 ± 0.05	0.05 ± 0.05
98 Ianthe	0.05 ± 0.05^d	0.05 ± 0.05	849 Ara	0.05 ± 0.05	0.05 ± 0.05
109 Felicitas	0.05 ± 0.05	0.05 ± 0.05	683 Lanzia	0.05 ± 0.05	0.05 ± 0.05
62 Erato	0.05 ± 0.05	0.05 ± 0.05	517 Edith	0.05 ± 0.05	0.05 ± 0.05
385 Ilmatar	0.05 ± 0.05	0.05 ± 0.05	83 Beatrix	0.05 ± 0.05	0.05 ± 0.05
160 Una	0.05 ± 0.05	0.05 ± 0.05	81 Terpsichore	0.05 ± 0.05^d	0.05 ± 0.05
740 Cantabia	0.05 ± 0.05	0.05 ± 0.05	206 Hersilia	0.05 ± 0.05	0.05 ± 0.05
791 Ani	0.05 ± 0.05	0.05 ± 0.05	358 Apollonia	0.05 ± 0.05	0.05 ± 0.05
663 Gerlinde	0.05 ± 0.05	0.05 ± 0.05	227 Philosophia	0.05 ± 0.05	0.05 ± 0.05
32 Pomona	0.05 ± 0.05	0.05 ± 0.05	554 Peraga	0.04 ± 0.05^d	0.04 ± 0.05
79 Eurynome	0.04 ± 0.04	0.04 ± 0.04	322 Phaeo	0.04 ± 0.04^d	0.04 ± 0.04
735 Marghanna	0.04 ± 0.04^d	0.04 ± 0.04	58 Concordia	0.04 ± 0.04	0.04 ± 0.04
195 Eurykleia	0.04 ± 0.04	0.04 ± 0.04	667 Denise	0.04 ± 0.04	0.04 ± 0.04
124 Alkeste	0.04 ± 0.04	0.04 ± 0.04	163 Erigone	0.04 ± 0.04^d	0.04 ± 0.04
568 Cheruskia	0.04 ± 0.04	0.04 ± 0.04	680 Genoveva	0.04 ± 0.04^d	0.04 ± 0.04
103 Hera	0.04 ± 0.04	0.04 ± 0.04	213 Lilaea	0.04 ± 0.04	0.04 ± 0.04
1107 Lictoria	0.04 ± 0.04	0.04 ± 0.04	691 Lehigh	0.04 ± 0.04	0.04 ± 0.04
205 Martha	0.04 ± 0.04	0.04 ± 0.04	72 Feronia	0.04 ± 0.04^d	0.04 ± 0.04
464 Megaira	0.04 ± 0.04	0.04 ± 0.04	362 Havnia	0.04 ± 0.04	0.04 ± 0.04
336 Lacadiera	0.03 ± 0.03	0.03 ± 0.03	598 Octavia	0.03 ± 0.03	0.03 ± 0.03
389 Industria	0.03 ± 0.03	0.03 ± 0.03	760 Massinga	0.03 ± 0.03^d	0.03 ± 0.03
569 Misa	0.03 ± 0.03	0.03 ± 0.03	431 Nephele	0.03 ± 0.03	0.03 ± 0.03
604 Tekmessa	0.03 ± 0.03^d	0.03 ± 0.03	53 Kalypso	0.03 ± 0.03^d	0.03 ± 0.03
1171 Rusthawelia	0.03 ± 0.03^d	0.03 ± 0.03	369 Aeria	0.03 ± 0.03	0.03 ± 0.03
112 Iphigenia	0.03 ± 0.03^d	0.03 ± 0.03	465 Alekto	0.03 ± 0.03	0.03 ± 0.03
1036 Ganymed	0.03 ± 0.03^d	0.03 ± 0.03	739 Mandeville	0.03 ± 0.03^d	0.03 ± 0.03
363 Padua	0.03 ± 0.03	0.03 ± 0.03	535 Montague	0.03 ± 0.03	0.03 ± 0.03
25 Phocaea	0.03 ± 0.03^d	0.03 ± 0.03	304 Olga	0.03 ± 0.03^d	0.03 ± 0.03
82 Alkmene	0.03 ± 0.03	0.03 ± 0.03	516 Amherstia	0.03 ± 0.03^d	0.03 ± 0.03
599 Luisa	0.03 ± 0.03	0.03 ± 0.03	43 Ariadne	0.03 ± 0.03^d	0.03 ± 0.03
99 Dike	0.03 ± 0.03	0.03 ± 0.03	424 Gratia	0.03 ± 0.03	0.03 ± 0.03
49 Pales	0.03 ± 0.03^d	0.03 ± 0.03	1021 Flammario	0.03 ± 0.03^d	0.03 ± 0.03
454 Mathesis	0.03 ± 0.03	0.03 ± 0.03	365 Corduba	0.03 ± 0.03^d	0.03 ± 0.03
337 Devosa	0.02 ± 0.02^d	0.02 ± 0.02	115 Thyra	0.02 ± 0.02	0.02 ± 0.02
415 Palatia	0.02 ± 0.02	0.02 ± 0.02	338 Budrosa	0.02 ± 0.02	0.02 ± 0.02
329 Svea	0.02 ± 0.02	0.02 ± 0.02	60 Echo	0.02 ± 0.02^d	0.02 ± 0.02
593 Titania	0.02 ± 0.02	0.02 ± 0.02	752 Sulamitis	0.02 ± 0.02	0.02 ± 0.02
44 Nysa	0.02 ± 0.02	0.02 ± 0.02	778 Theobalda	0.02 ± 0.02	0.02 ± 0.02
287 Nephthys	0.02 ± 0.02	0.02 ± 0.02	77 Frigga	0.02 ± 0.02^d	0.02 ± 0.02
914 Palisana	0.02 ± 0.02^d	0.02 ± 0.02	172 Baucis	0.02 ± 0.02	0.02 ± 0.02
75 Eurydike	0.02 ± 0.02	0.02 ± 0.02	177 Irma	0.02 ± 0.02	0.02 ± 0.02
485 Genua	0.02 ± 0.02^d	0.02 ± 0.02	224 Oceana	0.02 ± 0.02	0.02 ± 0.02
591 Irmgard	0.01 ± 0.01	0.01 ± 0.01	432 Pythia	0.01 ± 0.01	0.01 ± 0.01
584 Semiramis	0.01 ± 0.01^d	0.01 ± 0.01	198 Ampella	0.01 ± 0.01	0.01 ± 0.01
113 Amalthea	0.01 ± 0.01	0.01 ± 0.01	347 Pariana	0.01 ± 0.01	0.01 ± 0.01
547 Praxedis	0.01 ± 0.01	0.01 ± 0.01	118 Peitho	0.01 ± 0.01	0.01 ± 0.01
442 Eichsfeldia	0.01 ± 0.01^d	0.01 ± 0.01	132 Aethra	0.01 ± 0.01^d	0.01 ± 0.01
623 Chimaera	0.01 ± 0.01	0.01 ± 0.01	585 Bilkis	0.01 ± 0.01	0.01 ± 0.01
433 Eros	$0.0004463(1)^e$	0.0004463(1)			

References

Acton, C.H., 1996. Planet. Space Sci. 44, 65. http://dx.doi.org/10.1016/0032-0633(95)00107-7.

Acton, C., Bachman, N., Semenov, B., Wright, E., 2018. Planet. Space Sci. 150, 9. http://dx.doi.org/10.1016/j.pss.2017.02.013.

Baer, J., Chesley, S.R., 2017. Astron. J. 154, 76. http://dx.doi.org/10.3847/1538-3881/aa7de8.

Ballouz, R., 2017. Ph.D. thesis, University of Maryland, College Park.

Barnouin, O.S., Daly, M.G., Palmer, E.E., et al., 2019. Nat. Geosci. 12, 247. http://dx.doi.org/10.1038/s41561-019-0330-x.

Barnouin, O.S., Daly, M.G., Palmer, E.E., et al., 2020. Planet. Space Sci. 180, 104764. http://dx.doi.org/10.1016/j.pss.2019.104764.

Battin, R.H., 1987. An Introduction to the Mathematics and Methods of Astrodynamics. American Institute of Aeronautics and Astronautics.

Bertotti, B., Farinella, P., Vokrouhlický, D., 2003. Physics of the Solar System - Dynamics and Evolution, Space Physics, and Spacetime Structure. Springer Netherlands, http://dx.doi.org/10.1007/978-94-010-0233-2.

Bottke, W.F., Vokrouhlický, D., Rubincam, D.P., Nesvorný, D., 2006. Annu. Rev. Earth Planet. Sci. 34, 157. http://dx.doi.org/10.1146/annurev.earth.34.031405.125154.

Burns, J.A., Lamy, P.L., Soter, S., 1979. Icarus 40, 1. http://dx.doi.org/10.1016/0019-1035(79)90050-2.

Bus, S.J., Binzel, R.P., 2002. Icarus 158, 146. http://dx.doi.org/10.1006/icar.2002.6856.

Čapek, D., Vokrouhlický, D., 2004. Icarus 172, 526. http://dx.doi.org/10.1016/j.icarus.2004.07.003.

Čapek, D., Vokrouhlický, D., 2005. IAU Colloq. 197: Dynamics of Populations of Planetary Systems. pp. 171–178. http://dx.doi.org/10.1017/S1743921304008622.

Carry, B., 2012. Planet. Space Sci. 73, 98. http://dx.doi.org/10.1016/j.pss.2012.03.009.

Chesley, S.R., Chodas, P.W., Milani, A., Valsecchi, G.B., Yeomans, D.K., 2002. Icarus 159, 423. http://dx.doi.org/10.1006/icar.2002.6910.

Chesley, S.R., Farnocchia, D., Nolan, M.C., et al., 2014. Icarus 235, 5. http://dx.doi.org/10.1016/j.icarus.2014.02.020.

Chesley, S.R., Farnocchia, D., Pravec, P., Vokrouhlický, D., 2016. IAU Symp. 318: Asteroids: New Observations, New Models. pp. 250–258. http://dx.doi.org/10.1017/S1743921315008790.

Chesley, S.R., French, A.S., Davis, A.B., et al., 2020. J. Geophys. Res. (Planets) 125, e06363. http://dx.doi.org/10.1029/2019JE006363.

Christensen, P.R., Hamilton, V.E., Mehall, G.L., et al., 2018. Space Sci. Rev. 214, 87. http://dx.doi.org/10.1007/s11214-018-0513-6.

Daly, M.G., Barnouin, O.S., Seabrook, J.A., et al., 2020. Sci. Adv. 6, eabd3649. http://dx.doi.org/10.1126/sciadv.abd3649.

Del Vigna, A.., Faggioli, L., Milani, A., et al., 2018. Astronom. Astrophys. 617, A61. http://dx.doi.org/10.1051/0004-6361/201833153.

Eggl, S., Farnocchia, D., Chamberlin, A.B., Chesley, S.R., 2020. Icarus 339, 113596. http://dx.doi.org/10.1016/j.icarus.2019.113596.

Emery, J.P., Fernández, Y.R., Kelley, M.S.P., et al., 2014. Icarus 234, 17. http://dx.doi.org/10.1016/j.icarus.2014.02.005.

Farnocchia, D., Bellerose, J., Bhaskaran, S., Micheli, M., Weryk, R., 2021. Icarus 358, 114276. http://dx.doi.org/10.1016/j.icarus.2020.114276.

Farnocchia, D., Chesley, S.R., 2014. Icarus 229, 321. http://dx.doi.org/10.1016/j.icarus.2013.09.022.

Farnocchia, D., Chesley, S.R., Vokrouhlický, D., et al., 2013. Icarus 224, 1. http://dx.doi.org/10.1016/j.icarus.2013.02.004.
Farnocchia, D., Jenniskens, P., Robertson, D.K., et al., 2017a. Icarus 294, 218. http://dx.doi.org/10.1016/j.icarus.2017.03.007.
Farnocchia, D., Takahashi, Y., Chesley, S.R., et al., 2018. Tech. Rep. IOM 392R-18-005. Jet Propulsion Laboratory.
Farnocchia, D., Takahashi, Y., Chesley, S.R., et al., 2019. Lunar and Planetary Science Conference 50, 1512.
Farnocchia, D., Tholen, D.J., Micheli, M., et al., 2017b. AAS/Division for Planetary Sciences Meeting 49, 100.09.
Fedorets, G., Micheli, M., Jedicke, R., et al., 2020. Astron. J. 160, 277. http://dx.doi.org/10.3847/1538-3881/abc3bc.
Folkner, W.M., 2011. Tech. Rep. IOM 343R-11-003. Jet Propulsion Laboratory.
Folkner, W.M., Kahn, R.D., 1992. Tech. Rep. IOM 335.1-92-39. Jet Propulsion Laboratory.
Folkner, W.M., Williams, J.G., Boggs, D.H., Park, R.S., Kuchynka, P., 2014. Interplanetary Network Progress Report, 42-196.
Greenberg, A.H., Margot, J.-L., Verma, A.K., Taylor, P.A., Hodge, S.E., 2020. Astron. J. 159, 92. http://dx.doi.org/10.3847/1538-3881/ab62a3.
Gronchi, G.F., 2005. Celest. Mech. Dyn. Astron. 93, 295. http://dx.doi.org/10.1007/s10569-005-1623-5.
Gustafson, B.A.S., 1994. Annu. Rev. Earth Planet. Sci. 22, 553. http://dx.doi.org/10.1146/annurev.ea.22.050194.003005.
Hergenrother, C.W., Maleszewski, C., Li, J.Y., et al., 2020. J. Geophys. Res. (Planets) 125, e06381. http://dx.doi.org/10.1029/2020JE006381.
Hergenrother, C.W., Maleszewski, C.K., Nolan, M.C., et al., 2019. Nat. Commun. 10, 1291. http://dx.doi.org/10.1038/s41467-019-09213-x.
Kaula, W.M., 1966. Theory of Satellite Geodesy. Applications of Satellites To Geodesy. Dover Publications.
Konopliv, A.S., Asmar, S.W., Park, R.S., et al., 2014. Icarus 240, 103. http://dx.doi.org/10.1016/j.icarus.2013.09.005.
Krogh, F.T., 1974. Numerical Solution of Ordinary Differential Equations. pp. 22–71.
Lauretta, D.S., Balram-Knutson, S.S., Beshore, E., et al., 2017. Space Sci. Rev. 212, 925. http://dx.doi.org/10.1007/s11214-017-0405-1.
Lauretta, D.S., DellaGiustina, D.N., Bennett, C.A., et al., 2019a. Nature 568, 55. http://dx.doi.org/10.1038/s41586-019-1033-6.
Lauretta, D.S., Enos, H.L., Polit, A.T., Roper, H.L., Wolner, C.W.V., 2021. Sample Return Missions. http://dx.doi.org/10.1016/C2018-0-03374-5, (Chapter 8).
Lauretta, D.S., Hergenrother, C.W., Chesley, S.R., et al., 2019b. Science 366, 3544. http://dx.doi.org/10.1126/science.aay3544.
Lauretta, D.S., OSIRIS-REx TAG Team, 2021. Lunar and Planetary Science Conference 52, 2097.
Lemoine, F.G., Kenyon, S.C., Factor, J.K., et al., 1998. Tech. Rep. NASA/TP1998-206861. NASA Goddard Space Flight Center.
Lieske, J.H., 1977. Astronom. Astrophys. 56, 333.
Micheli, M., Tholen, D.J., Elliott, G.T., 2012. New Astron. 17, 446. http://dx.doi.org/10.1016/j.newast.2011.11.008.
Micheli, M., Tholen, D.J., Elliott, G.T., 2013. Icarus 226, 251. http://dx.doi.org/10.1016/j.icarus.2013.05.032.
Micheli, M., Tholen, D.J., Elliott, G.T., 2014. Astrophys. J. Lett. 788, L1. http://dx.doi.org/10.1088/2041-8205/788/1/L1.
Milani, A., Chesley, S.R., Sansaturio, M.E., et al., 2009. Icarus 203, 460. http://dx.doi.org/10.1016/j.icarus.2009.05.029.
Mommert, M., Farnocchia, D., Hora, J.L., et al., 2014b. Astrophys. J. Lett. 789, L22. http://dx.doi.org/10.1088/2041-8205/789/1/L22.
Mommert, M., Hora, J.L., Farnocchia, D., et al., 2014a. Astrophys. J. 786, 148. http://dx.doi.org/10.1088/0004-637X/786/2/148.
Moyer, T.D., 2003. Formulation for Observed and Computed Values of Deep Space Network Data Types for Navigation. Wiley-Interscience, Hoboken, NJ.
Nolan, M.C., Magri, C., Howell, E.S., et al., 2013. Icarus 226, 629. http://dx.doi.org/10.1016/j.icarus.2013.05.028.
Ostro, S.J., Hudson, R.S., Benner, L.A.M., et al., 2002. Asteroids III. pp. 151–168.
Owen, W.M., 2011. AAS/Spaceflight Mechanics Conference 21, 11-215.
Park, R.S., Folkner, W.M., Williams, J.G., Boggs, D.H., 2021. Astron. J. 161, 105. http://dx.doi.org/10.3847/1538-3881/abd414.
Park, R.S., Konopliv, A.S., Bills, B.G., et al., 2016. Nature 537, 515. http://dx.doi.org/10.1038/nature18955.
Pitjeva, E.V., Pitjev, N.P., Pavlov, D.A., Turygin, C.C., 2021. Astronom. Astrophys. 647, A141. http://dx.doi.org/10.1051/0004-6361/202039893.
Reuter, D.C., Simon, A.A., Hair, J., et al., 2018. Space Sci. Rev. 214, 54. http://dx.doi.org/10.1007/s11214-018-0482-9.
Rozitis, B., Green, S.F., 2011. Mon. Not. R. Astron. Soc. 415, 2042. http://dx.doi.org/10.1111/j.1365-2966.2011.18718.x.
Rozitis, B., Green, S.F., 2012. Mon. Not. R. Astron. Soc. 423, 367. http://dx.doi.org/10.1111/j.1365-2966.2012.20882.x.
Rozitis, B., Green, S.F., 2013. Mon. Not. R. Astron. Soc. 433, 603. http://dx.doi.org/10.1093/mnras/stt750.
Rozitis, B., Ryan, A.J., Emery, J.P., et al., 2020. Sci. Adv. 6, eabc3699. http://dx.doi.org/10.1126/sciadv.abc3699.
Scheeres, D.J., French, A.S., Tricarico, P., et al., 2020a. Sci. Adv. 6, eabc3350. http://dx.doi.org/10.1126/sciadv.abc3350.
Scheeres, D.J., McMahon, J.W., Brack, D.N., et al., 2020b. J. Geophys. Res. (Planets) 125, e06284. http://dx.doi.org/10.1029/2019JE006284.
Scheeres, D.J., McMahon, J.W., French, A.S., et al., 2019. Nat. Astron. 3, 352. http://dx.doi.org/10.1038/s41550-019-0721-3.
Seidelmann, P.K., 1977. Celest. Mech. 16, 165.
Standish, E.M., 1990. Astronom. Astrophys. 233, 252.
Tedesco, E.F., Noah, P.V., Noah, M., Price, S.D., 2002. Astron. J. 123, 1056. http://dx.doi.org/10.1086/338320.
Thornton, C.L., Border, J.S., 2003. Radiometric Tracking Techniques for Deep-Space Navigation. Wiley, Hoboken, NJ.
Valsecchi, G.B., Milani, A., Gronchi, G.F., Chesley, S.R., 2003. Astronom. Astrophys. 408, 1179. http://dx.doi.org/10.1051/0004-6361:20031039.
Vereš, P., Farnocchia, D., Chesley, S.R., Chamberlin, A.B., 2017. Icarus 296, 139. http://dx.doi.org/10.1016/j.icarus.2017.05.021.
Vokrouhlický, D., Bottke, W.F., Chesley, S.R., Scheeres, D.J., Statler, T.S., 2015. Asteroids IV. pp. 509–531. http://dx.doi.org/10.2458/azu_uapress_9780816532131-ch027.
Vokrouhlický, D., Milani, A., 2000. Astronom. Astrophys. 362, 746.
Vokrouhlický, D., Milani, A., Chesley, S.R., 2000. Icarus 148, 118. http://dx.doi.org/10.1006/icar.2000.6469.
Wiegert, P.A., 2015. Icarus 252, 22. http://dx.doi.org/10.1016/j.icarus.2014.12.022.
Will, C.M., 1993. Theory and Experiment in Gravitational Physics. Cambridge University Press.
Yeomans, D.K., Antreasian, P.G., Barriot, J.P., et al., 2000. Science 289, 2085. http://dx.doi.org/10.1126/science.289.5487.2085.
Yeomans, D.K., Ostro, S.J., Chodas, P.W., 1987. Astron. J. 94, 189. http://dx.doi.org/10.1086/114463.